CDDpress

www.nature.com/cdd

ARTICLE

Check for updates

Small extracellular vesicles delivering lncRNA WAC-AS1 aggravate renal allograft ischemia–reperfusion injury by inducing ferroptosis propagation

Xinyuan Li[1,2,3,4], Xiang Peng[1,3,4], Xiang Zhou[1,3,4], Mao Li[1], Guo Chen[1,3], Wei Shi[1,3], Haitao Yu[1,3], Chunlin Zhang[1,3], Yang Li[1,3], Zhenwei Feng[1,3], Jie Li[1], Simin Liang[1], Weiyang He[1✉] and Xin Gou[1✉]

Ferroptosis is a predominant contributor to renal ischemia reperfusion injury (IRI) after kidney transplant, evoking delayed graft function and poorer long-term outcomes. The wide propagation of ferroptosis among cell populations in a wave-like manner, developing the "wave of ferroptosis" causes a larger area of tubular necrosis and accordingly aggravates renal allograft IRI. In this study, we decipher a whole new metabolic mechanism underlying ferroptosis and propose a novel spreading pathway of the "wave of ferroptosis" in the renal tissue microenvironment, in which renal IRI cell-secreted small extracellular vesicles (IRI-sEVs) delivering lncRNA WAC-AS1 reprogram glucose metabolism in adjacent renal tubular epithelial cell populations by inducing GFPT1 expression and increasing hexosamine biosynthesis pathway (HBP) flux, and consequently enhances O-GlcNAcylation. Additionally, BACH2 O-GlcNAcylation at threonine 389 in renal tubular epithelial cells prominently inhibits its degradation by ubiquitination and promotes importin α5-mediated nuclear translocation. We present the first evidence that intranuclear BACH2 suppresses SLC7A11 and GPX4 transcription by binding to their proximal promoters and decreases cellular anti-peroxidation capability, accordingly facilitating ferroptosis. Inhibition of sEV biogenesis and secretion by GW4869 and knockout of lncRNA WAC-AS1 in IRI-sEVs both unequivocally diminished the "wave of ferroptosis" propagation and protected against renal allograft IRI. The functional and mechanistic regulation of IRI-sEVs was further corroborated in an allograft kidney transplant model and an in situ renal IRI model. In summary, these findings suggest that inhibiting sEV-mediated lncRNA WAC-AS1 secretion and targeting HBP metabolism-induced BACH2 O-GlcNAcylation in renal tubular epithelial cells may serve as new strategies for protecting against graft IRI after kidney transplant.

Cell Death & Differentiation; https://doi.org/10.1038/s41418-023-01198-x

INTRODUCTION

Due to several episodes of cold and warm ischemia during procurement, storage and transplantation processes in allograft renal transplant surgery, ischemia–reperfusion injury (IRI) is an inevitable consequence, consequently provoking delayed graft function (DGF), structural damage and even systemic complications [1–3]. In addition, the current enormous imbalances of supply and demand cause an increased use of marginal donor kidneys, including donation after circulatory death and donors meeting extended criteria, further exacerbating IRI-induced DGF [4]. Therefore, a deeper understanding of IRI mechanisms and patterns remains warranted to explore novel therapeutic targets and accurate biomarkers for prognostic estimation.

There is currently soaring evidence corroborating that ferroptosis, unique among all main cell death modalities discovered to date, is the dominant driving force mediating renal IRI [5, 6]. Interestingly, recent studies describe a novel and devastating phenomenon of the "wave of ferroptosis" in the process of renal IRI; that is, ferroptosis has the unusual ability to widely spread through renal tubular epithelial cells in a successive manner, with an expanding scale and wave-like appearance, thereby eliminating entire cell populations and evoking large and continuous areas of tubular necrosis [6–8]. However, the propagating approaches and regulatory mechanisms of the "wave of ferroptosis" remain incompletely understood. Linkermann [8], Massenhausen [9], Vanden Berghe [10] et al. demonstrated that dying cell-derived nicotinamide adenine dinucleotide phosphate (NADPH) diffusion in the tubular compartment renders neighboring cells susceptible to ferroptosis. Interestingly, the team of Michael Overholtzer recently proposed a novel mechanism whereby intercellular nanoparticle-delivering iron induced ferroptosis spreading between starved cell populations in a wave-like manner and inhibited tumor growth [11]. In addition, Brown et al. found that cells under ferroptotic signal stimuli suppressed the onset of ferroptosis by secreting exosome trafficking iron out of the cell [12]. On these interesting premises that nanoparticles modulate ferroptotic development and propagation, we further raise a potential possibility, for the first time, that IRI cell-derived small

[1]Department of Urology, The First Affiliated Hospital of Chongqing Medical University, Chongqing, China. [2]CAS Center for Excellence in Molecular Cell Science, Shanghai Institute of Biochemistry and Cell Biology, Chinese Academy of Sciences, Shanghai, China. [3]Chongqing Key Laboratory of Molecular Oncology and Epigenetics, Chongqing, China. [4]These authors contributed equally: Xinyuan Li, Xiang Peng, Xiang Zhou. ✉email: weiyang361@163.com; gouxincq@163.com

Received: 7 March 2023 Revised: 11 July 2023 Accepted: 20 July 2023
Published online: 02 August 2023

extracellular vesicles (IRI-sEVs), also a type of nanoparticle with a lipid bilayer, mediate ferroptosis spread among neighboring cells and generate a "wave of ferroptosis" in the renal tissue microenvironment during the IRI process.

SEVs, as a heterogeneous population of nanoscale vesicles with a diameter of approximately 30–200 nm, have been well documented to mediate intercellular and interorgan communication and induce genetic and functional alterations in recipient cells as systemic messengers delivering signaling molecules [13–15]. There have been overwhelming studies in the last few years indicating the prominent roles of sEVs in IRI; nevertheless, the vast majority of these studies have focused on the therapeutic effects of stem cell-derived sEVs through various mechanisms, such as anti-inflammatory, anti-apoptotic, antioxidant, tissue repair and immunomodulatory mechanisms [16–18]. However, only a few researchers have reported sEV-mediated damage, including aggravating organ IRI and inducing remote organ injury, and even fewer reports have examined the aggressive functions of IRI-sEVs on adjacent uninjured cells and distant organs. Gan et al. reported that miR-130b-3p enriched in dysfunctional adipocyte-secreted sEVs aggravated myocardial IRI by decreasing a diverse array of cardioprotective molecules in cardiomyocytes [18]. In addition, Ge et al. demonstrated that -derived detrimental sEVs not only exacerbated local sterile inflammation in the myocardia itself but also mediated kidney-lung crosstalk and provoked systemic inflammation in the lung [19]. Nevertheless, whether and how IRI-sEVs exert their effects during the renal IRI process, especially in "wave of ferroptosis" propagation, remain less clear-cut.

Renal tubular epithelial cells face multiple challenging stress conditions during the IRI process, such as oxygen-glucose deprivation. As a prerequisite of cellular activities, glucose metabolism not only produces adenosine triphosphate for energetic support but also provides precursors for indispensable macromolecule biosynthesis [20]. Emerging evidence has revealed that a series of glucose-related metabolic pathways, such as glycolysis [21, 22], the pentose phosphate pathway (PPP) [23, 24], oxidative phosphorylation (OXPHOS) [25, 26] and the tricarboxylic acid (TCA) cycle [22], play crucial roles in ferroptosis by regulating cellular antioxidative defense. Nevertheless, in contrast to the extensive understanding of how glucose metabolic reprogramming modulates ferroptosis, little is known about the role of the hexosamine biosynthetic pathway (HBP), another branch of glucose metabolism, in regulating ferroptosis.

HBP metabolism branching off from fructose 6-phosphate in glucose metabolism forms an integral metabolic node and fuels the synthesis of uridine diphosphate-N-acetylglucosamine (UDP-GlcNAc), a major substrate for O-linked-N-acetylglucosamine (O-GlcNAc) protein modification (O-GlcNAcylation) [27]. Glutamine-fructose-6-phosphate aminotransferase 1 (GFPT1), acting as a rate-limiting switch in the HBP, increases HBP fluxes by accelerating the shunting of fructose 6-phosphate to glucosamine 6-phosphate, thereby heightening the level of O-GlcNAc posttranslational modification [28]. Many studies have revealed the pivotal role of HBP-mediated O-GlcNAcylation in a diverse array of diseases, including malignant tumors and organ IRI injury. For example, in acute myocardial infarction, Mapanga et al. demonstrated that hyperglycemia prominently induced myocardial oxidative stress and increased HBP fluxes, leading to further cardiac dysfunction [29, 30]. However, the results of Cong's study suggested that an acute increase in protein O-GlcNAcylation conferred robust protection against IR-induced intestinal injury and could be a promising therapeutic strategy for intestinal IRI [31]. This notwithstanding, there are still numerous open gaps in the understanding of whether HBP metabolism and O-GlcNAcylation affect ferroptosis in renal IRI, as does the question of whether IRI-sEVs mediate HBP metabolic reprogramming in neighboring cells, thus inducing a "wave of ferroptosis".

Here, for the first time, we confirmed the crucial role of IRI-sEVs in promoting the "wave of ferroptosis" propagation and thereby exacerbating tubular necrosis during the renal IRI process. In addition, we identified that long non-coding RNA WAC-AS1 (lncRNA-WAC-AS1) enriched in IRI-sEVs prominently increased HBP metabolic fluxes by upregulating GFPT1 and promoted BACH2 O-GlcNAcylation in normal renal tubular epithelial cell populations, thus suppressing the transcriptional activities of SLC7A11 and GPX4 and inducing ferroptosis. These results reveal a whole new propagative approach and metabolic mechanism underlying the "wave of ferroptosis" in the renal IRI process and imply that lncRNA-WAC-AS1 is a novel biomarker and potential target for the early evaluation and treatment of IRI after kidney transplantation.

METHODS

Human study

Forty-seven donor kidneys from twenty-nine donors were transplanted to forty-seven patients who underwent allograft kidney transplant surgery at the First Affiliated Hospital of Chongqing Medical University (Table 1). These donor-recipient pairs were included in the study, and their urine samples were obtained for sEV separation. The clean and fresh urine of the donor (100 mL) was collected one hour before donor kidney excision, and urine produced from the posttransplant kidney in the recipient (100 mL) was harvested at one and two days after surgery. Informed written consent was obtained from all participants and (or) relatives. The study was approved by the Medical Ethics Committee of the First Affiliated Hospital of Chongqing Medical University (181). All included clinical data were carefully reviewed in reference to medical records. The clinical and research activities being reported are consistent with the Principles of the Declaration of Istanbul as outlined in the "Declaration of Istanbul on Organ Trafficking and Transplant Tourism".

Animals

C57BL/6-Gfat1$^{+/-}$ mice were obtained from AAALCA-accredited MODEL ORGANISMS (Shanghai, CHN) and were crossed to generate GFAT1 global knockout mice (C57BL/6-Gfat1$^{-/-}$, GFKO). Male GFKO mice and wild-type C57BL/6 mice (WT) aged 8–10 weeks were used for experiments. All mice were housed at the standardized animal facility with constant temperature and humidity and a 12-h light/12-h dark cycle in the Animal Centre of Chongqing Medical University and regularly monitored by a certified veterinarian. All animal experimental protocols and care procedures conformed to the Chongqing Medical University of Medicine Policy on the Care and Use of Laboratory Animals (k276). Random allocation of animals was conducted by computer-generated random numbers. Investigators were blinded to group allocation during data collection and analysis.

Mouse model of allograft kidney transplantation

Kidney transplantation between syngeneic mice was conducted following procedures described previously with minor modifications [2]. Donor mice were anesthetized with pentobarbital (50 mg/kg, intraperitoneally) and kept on a thermostatic insulation pad to maintain body temperature, and the right kidney was excised and stored in 4 °C cold Ringer lactate solution for 6 h (cold ischemia). Under general anesthesia, the recipient underwent right-sided nephrectomy and then completed orthotopic donor-recipient kidney vascular anastomosis using 10-0 silk sutures within 30 min (warm ischemia). Next, the ureter was fixed to the bladder lateral wall. Finally, the contralateral native kidney (left kidney) of the recipient was removed, and the abdomen was closed with 4-0 silk suture. During the entire process of kidney transplantation, the recipient was placed on a heating pad for temperature maintenance and kept intraperitoneally moist by instilling warm normal saline (NS, Beyotime, CHN). Recipient mice were euthanized according to the guidelines set forth by the American Veterinary Medicine Association at 2 days posttransplantation to procure blood, kidney and remote organs for sEV separation, biochemistry detection and other relative assays.

For inhibition of sEV biogenesis and secretion, GW4869 (MCE, CHN) was injected intraperitoneally at 2.5 mg/kg into donor and recipient mice in the KT + GW4869 group 1 h before donor kidney excision and kidney transplantation, and mice in other groups received equal DMSO

Table 1. Clinical characteristics of kidney pairs included in the study.

Kidney pair ID		Age (year)		Doner type	Cold ischemia time	HLA mismatch number	Kidney weight (g)	DDS	Nyberg grade
Doner	Recipient	Doner	Recipient						
1	1	26	22	CVM	12 h 10 min	3	L-270	7	A
	2		35			3	R-275	7	A
2	1	59	59	ICH	4 h 15 min	6	L-225	23	C
	2		51			5	R-215	23	C
3	2	50	28	NCD	6 h	1	R-220	18	B
4	1	54	50	ICH	3 h 35 min	1	L-260	22	C
	2		31			2	R-260	23	C
5	2	34	43	ICH	9 h 40 min	4	L-295	10	B
6	2	22	25	CVM	4 h 50 min	5	L-280	6	A
7	2	51	44	ICH	6 h 20 min	4	L-245	22	C
8	2	50	51	ICH	6 h 5 min	6	R-210	24	C
9	1	41	54	ICH	8 h 55 min	5	L-255	18	B
	2		56			6	R-250	18	B
10	1	42	60	NCD	4 h 10 min	6	R-245	13	B
11	1	21	15	NCD	4 h 5 min	5	L-230	3	A
	2		49			2	R-230	1	A
12	1	46	52	NCD	4 h 35 min	2	L-285	13	B
	2		43			1	R-275	13	B
13	1	32	36	NCD	5 h 10 min	5	R-265	8	A
14	1	46	37	ICH	10 h 10 min	4	L-230	17	B
	2		47			5	R-240	18	B
15	1	29	53	NCD	6 h 5 min	5	L-275	3	A
	2		56			6	R-270	3	A
16	1	67	54	NCD	4 h 15 min	3	R-290	26	C
17	1	35	30	CHP	3 h 30 min	2	L-265	9	A
	2		63			1	R-270	9	A
18	1	57	55	NCD	11 h 15 min	4	L-245	20	C
19	1	50	39	CVM	8 h 45 min	6	L-220	24	C
	2		31			6	R-220	24	C
20	1	44	58	NCD	10 h 25 min	3	R-255	14	B
21	1	40	56	NCD	7 h 20 min	4	L-270	14	B
	2		68			4	R-265	14	B
22	1	60	65	ICH	4 h 55 min	6	L-280	32	D
	2		69			3	R-280	31	D
23	1	33	59	ICH	10 h	6	L-235	13	B
	2		30			5	R-235	13	B
24	1	58	49	ICH	4 h 10 min	5	L-250	24	C
	2		52			6	R-250	24	C
25	1	49	41	NCD	4 h 30 min	3	L-275	12	B
	2		34			5	R-280	13	B
26	1	49	50	ICH	9 h 20 min	3	L-240	20	C
	2		22			2	R-250	19	B
27	2	34	31	NCD	4 h 10 min	5	L-265	10	B
28	1	48	38	NCD	9 h 55 min	2	L-270	11	B
	2		27			2	R-270	11	B
29	1	15	44	NCD	6 h 45 min	5	L-295	3	A
	2		46			3	R-285	2	A

CHP communicating hydrocephalus, *CVM* cerebrovascular malformation, *DDS* deceased donor score (Nyberg grade A: 0–9, Nyberg grade B: 10–19, Nyberg grade C: 20–29, Nyberg grade D: 30–39; non-marginal donor kidney: Nyberg grade A and B, marginal donor kidney: Nyberg grade C and D), *HLA* human leucocyte antigen, *ICH* intracerebral hemorrhage, *L* left kidney, *R* right kidney, *NCD* non-cerebrovascular disease.

(Sigma–Aldrich, CHN) intervention as a control. To suppress ferroptosis, donor and recipient mice in the KT + $csEVs_{WT}$ + Fer-1 group received intraperitoneal injection of ferrostatin-1 (5 mg/kg, Sigma–Aldrich, CHN) in parallel to the treatment timing of GW4869. The sEV treatment models were established by tail intravenous injection of 100 μg of different HK-2 cell-derived sEVs or NS (as control) at the very beginning of reperfusion and 1 day postsurgery.

In situ kidney IRI model

To establish an in situ kidney warm ischemia–reperfusion model in vivo, WT and GFKO mice were anesthetized and placed on a thermostatic insulation pad. Following left-side nephrectomy, the right renal pedicle was occluded with a small microvascular clamp to induce warm ischemia for 35 min, and then a release clamp was used for reperfusion. Mice in the sham group underwent the same procedure but without pedicle clamping. Finally, the small incision was closed using 4-0 silk suture. Mice were euthanized to procure blood and the right kidney 1 day after reperfusion.

Cell culture and treatment

The HK-2 human proximal tubular cell line and human embryonic kidney cell line (293T) were purchased from the Cell Bank of the Chinese Academy of Sciences (Shanghai, China) and cultured in Dulbecco's modified Eagle's medium (DMEM)/F12 (Gibco, USA) and DMEM (Gibco, USA), respectively, containing 10% fetal bovine serum (FBS, BioInd, Israel), 100 μg/mL streptomycin (Beyotime, CHN), and 100 U/mL penicillin (Beyotime, CHN) at 37 °C in a humidified atmosphere of 5% CO_2. Cell lines have been tested for mycoplasma contamination. To establish in vitro sEV-administration models, 30 μg of cell supernatant or urine-derived sEVs were supplemented into the complete medium of 10^6 HK-2 cells for 24 h. In addition, cells were treated with GW4869 (20 μM), ferrostatin-1 (1 μM), erastin (10 μM, Sigma–Aldrich, CHN), PUGNAc (50 μM, Sigma–Aldrich, CHN) or OSMI-1 (50 μM, Sigma–Aldrich, CHN), as indicated.

In vitro IRI model

Oxygen-glucose deprivation, a type of chemical anoxia/recovery method, was utilized to establish an in vitro IRI model, as previously described. In brief, HK-2 cells were cultivated in glucose-free medium supplemented with antimycin A (5 μM)/2-deoxyglucose (5 mM) to simulate the ischemic process for 1 h, then the medium was replaced with complete medium, and the cells entered a reperfusion phase for 24 or 48 h.

Generation of stable cell lines with lentivirus and CRISPR–Cas9 systems

To construct cell lines with stable overexpression of lncRNA-WAC-AS1 (WOE) and BACH2 (BOE), lentivirus vectors (pLVX/PGK/Puro and pGLV5/Puro) containing their full-length cDNA fragments were transfected into different HK-2 cells, followed by puromycin (5 μg/mL) screening for 2 weeks. HK-2 cells transfected with empty vector were used as a control (WT). In addition, individual guide sequences targeting lncRNA-WAC-AS1 and GFPT1 were cloned into pSpCas9 BB-2A-Puro (PX459) to establish a lncRNA-WAC-AS1 knockout cell line (WKO) using the CRISPR–Cas9 system, as previously described [32]. The GAL4-guide sequence was subcloned into the PX459 vector as a control (WT). The sequences of oligonucleotides are listed in Supplementary File 1: Supplementary Table S1.

Oligonucleotides, plasmids, siRNA and cell transfection

Full-length cDNA, cDNA encoding certain residues and mutant cDNA of O-GlcNAc transferase (OGT), BACH2, ubiquitin (Ub) and karyopherin subunit alpha 1 (KPNA1) were separately subcloned into the pcDNA 3.1 plasmid or pEGFP-N1 plasmid with different tags as indicated. Mimic NC, microRNA-369–3p (miR-369–3p) mimic, miR-449b-5p mimic, inhibitor NC, miR-369–3p inhibitor, miR-449b-5p inhibitor and siRNA-BACH2 were synthesized by Tsingke Biotechnology Co., Ltd. (CHN). Plasmids were validated by DNA sequencing, and oligonucleotides were transfected utilizing Lipofectamine 3000 Transfection Reagent (Invitrogen, USA) according to the manufacturer's instructions.

Separation and concentration of sEVs from cell medium, urine, serum and tissue

Differential ultracentrifugation (UC) was utilized to separate sEVs from the cell medium (csEVs) according to the guidelines of MISEV2018 of the Journal of Extracellular Vesicles [33]. Cells were cultured in EV-free complete medium, of which EVs were depleted by UC at 140,000 × *g* for 18 h in advance (Type 45 Ti rotor, k-Factor 217.6, Beckman Coulter, USA). After different treatments, the conditioned medium was collected when cells reached 80–90% confluency with an approximately 5–20% death rate. For sEV separation, cells and cellular debris were first eliminated from the cell medium through sequential centrifugation steps of 300 × *g* for 10 min, 2000 × *g* for 20 min, and 12,000 × *g* and 4 °C for 30 min, followed by gravitational filtration utilizing a 0.22-μm hydrophilic syringe filter (Millipore, MA, USA). Next, sEVs were pelleted from the above resulting medium through two consecutive UC steps separately lasting 70 min at 140,000 × *g* (Type 45 Ti rotor, adjusted k-Factor 133, maximal acceleration, maximal deceleration). Finally, csEVs were resuspended in 150 μL of sterile phosphate-buffered saline (PBS) for follow-up experiments or stored at −80 °C. The freezing-thawing cycle was performed not more than one time.

Urine-derived sEVs (usEVs) were separated and concentrated by OptiPrep density gradient (ODG) ultracentrifugation as previously described [34]. For urine sample preprocessing, clean and fresh urine samples from the donor and recipient were briefly precleaned by two successive centrifugation steps at 2000 × *g* for 20 min and 12,000 × *g* and 4 °C for 30 min, followed by a filtering step using a 0.22-μm hydrophilic syringe filter. The prepared urine specimens were utilized for usEV isolation or stored at −80 °C. For ODG ultracentrifugation, 50-mL urine samples were first concentrated to 500–800 μL by a 10 kDa centrifugal filter device (Centricon Plus-70, Merck Millipore) and then diluted with Tris buffer (10 mM Tris-HCl, pH: 7.4, 1 mM EDTA and 0.25 M sucrose) to a volume of 800 μL, which was prepared as a 40% iodixanol suspension by mixing with a 3.2-mL working solution (0.25 M sucrose, 6 mM EDTA, 60 mM Tris-HCl, pH: 7.4). Next, a 17-mL thinwall polypropylene tube (Beckman Coulter, USA) was discontinuously bottom-up filled with 4 mL of 40% iodixanol suspension, 4 mL of 20% iodixanol, 4 mL of 10% iodixanol, 3.5 mL of 5% iodixanol and 1 mL of PBS to build an ODG system. After centrifugation at 100,000 × *g* and 4 °C for 18 h (SW 32.1 Ti rotor with ravg = 11.36 cm, adjusted k-factor = 298.0, maximal acceleration, maximal deceleration), the 6^{th}–10^{th} fractions (1 mL) were separately top-down harvested to a new tube, and the final volume was brought to 16 mL with PBS for subsequent centrifugation at 100,000 × *g* and 4 °C for 3 h. The usEV pellets were resuspended in 150 μL of sterile PBS for subsequent analyses or stored in the same manner as csEVs.

Tissue-derived sEVs (tsEVs) were also isolated and concentrated through UC as previously described with minor modifications [35]. Mouse renal tissues were gently dissociated into approximately 1-mm^3 pieces, followed by enzymatic digestion in Hank's equilibrium salt solution (HBSS, Thermo Fisher Scientific, USA) supplemented with 1 mg/mL collagenase type 4 (Worthington, USA) and 30 U/mL DNase I (Sigma–Aldrich, CHN) for 1 h on a rotor at 37 °C. Then, the tissue suspension mixed with precooled HBSS was sequentially filtered through a 70-mm Cell-Strainer (BD, USA) for tsEV separation by UC, in line with the isolation steps of csEVs.

Dichotomic size-exclusion chromatography (SEC) was utilized to separate and concentrate mouse serum-derived sEVs (ssEVs) as previously described with minor modifications [36]. Fresh whole blood samples (4–6 mL) were centrifuged at 1000 × *g* for 10 min to separate serum, which was sequentially centrifuged at 2500 × *g* for 20 min and 10,000 × *g* at 4 °C for 20 min to eliminate cells, fragments, platelets and other non-EV components. The well-prepared serum was directly isolated from ssEVs or stored at −80 °C. For ssEV separation, 1-2-mL serum samples were loaded into the prepared SEC column system consisting of an SEC column packed with CL-6B resins (Senbeijia Biological Technology Co., Ltd., China) and an Econo-Pac chromatography column (Bio-Rad Laboratories, Inc., China) to be fractionated, followed by elution using sterile PBS. The first 5 mL of eluent was discarded, and the next 6–9 mL of eluent containing the majority of ssEVs was collected as Elution 1. Elution 2, the next 17-mL eluent, was used as a control. Then, elution 1 was concentrated to 200 μL through an Amicon ultra4 filter equipped with a 30-kDa molecular-weight cutoff membrane (Sartorius, GER), combined with centrifugation at 4000 × *g* (35° fixed angle rotor). The final concentrates were used for subsequent experiments or stored at −80 °C until use. The freezing-thawing cycle was performed not more than one time. Frozen serum samples were centrifuged at 17,000 × *g* and 4 °C for 10 min to deplete the aggregates in advance.

Transmission electron microscopy

The morphology of sEVs was observed by transmission electron microscopy (TEM, Hitachi-7500, Yokohama, Japan). Briefly, sEVs were fixed

with 0.5% glutaraldehyde solution overnight and centrifuged at 13,000 × *g* for 3 min to discard the supernatant. After dehydration in absolute ethanol for 10 min, the sEV sample was dropped onto a 100-mesh formvar-carbon-coated copper grid (TED PELLA, Inc., USA) and dried by filter paper after 10 min. Afterward, the grate was stained with 1% phosphotungstic acid for 30 s, washed twice with absolute ethanol and completely dried at room temperature.

Flow NanoAnalyzer

The high-resolution size distribution of sEV was measured by Flow NanoAnalyzer in a NanoFCM system (NanoFCM, CHN).

Tracking of sEVs

The sEV trace in vitro was visualized by using the PKH67 (Sigma–Aldrich, CHN) label. PKH67-labeled sEVs (30 μg) were added to the complete medium of HK-2 cells for 6 h, with PBS supplement serving as a negative control, followed by scanning under a laser confocal microscope (Leica Microsystems AG). In addition, PKH26 (Sigma–Aldrich, CHN) was utilized to label sEVs for tracking in vivo. After tail intravenous injection of 100 μg of PKH26-labeled sEVs or NS (as control) for 2 h and 6 h, the mice were anesthetized and imaged using an IVIS Lumina imaging system (Caliper Life Sciences, USA).

Whole transcriptome sequencing of usEVs

Total RNA in usEVs was isolated using an exoRNeasy Serum/Plasma Maxi kit (Qiagen, GER) following the manufacturer's instructions. The Illumina-compatible RNA-seq libraries were generated by a SMARTer Stranded Total RNA-Seq Kit v2 (Takara Bio, USA). First, total RNA was fragmented into a size appropriate for sequencing on Illumina platforms and converted to first-strand cDNA. Then, adapters for Illumina sequencing (with specific barcodes) were added through PCR using only a limited number of cycles to distinguish pooled libraries from each other after sequencing. Following the purification of amplified RNA-seq libraries by immobilization onto AMPure beads, the library fragments originating from rRNA (18S and 28S) and mitochondrial rRNA (m12S and m16S) were cut by ZapR v2 in the presence of R-Probes v2 (mammalian-specific). Next, the library fragments that were not cleaved by the ZapR v2 reaction were further amplified with primers universal to all libraries. Finally, the amplified RNA-seq library was purified by immobilization onto AMPure beads once more to yield cDNA libraries for sequencing on Illumina platforms.

Metabolite detection by LC–MS/MS analysis

The cell and tissue samples were thawed, smashed and resuspended in a 500-μL precooled buffer containing equal volumes of methanol and acetonitrile (Merck, GER). Then, 300 μL of supernatant was obtained following low-temperature centrifugation at 14,000 × *g* for 20 min and incubated in a −20 °C refrigerator for 30 min. Afterward, the cooled supernatant was centrifuged under the same conditions again to harvest the supernatant, of which 200 μL was transferred to a protein precipitation plate and further assessed by LC–MS analysis based on the AB Sciex QTRAP 6500 LC–MS/MS platform.

O-GlcNAcylated protein identification by LC–MS/MS analysis

The protein samples of renal tissues were extracted, quantified and digested for peptide preparation. Following reconstitution in IAP buffer (Cell Signaling Technology, CST, USA), the peptide solution was adequately mixed with prewashed anti-GlcNAc-S/T antibody beads (CST, USA) and incubated at 4 °C overnight for O-GlcNAcylated peptide enrichment. Next, beads were washed with 1 mL of precooled IAP buffer and tri-distilled water 3 times each, followed by incubation with 40 μL of 0.15% TFA (Sigma–Aldrich, CHN) for 10 min at room temperature (mixed gently every 3 min). After supplementation with 0.15% TFA twice, the supernatant was harvested by centrifugation (2000 × *g*, 30 s) for further desalting treatment. The processed samples were detected by LC–MS/MS analysis on a timsTOF Pro mass spectrometer coupled to nanoElute (Bruker Daltonics, GER). In addition, Peaks (BSI, CAN) was employed for the raw MS data analyses.

BACH2 protein stability assay

HK-2 cells transfected with plasmids containing HA-fusion BACH2 full-length cDNA (BACH2-HA) or a mutation at threonine 389 (BACH2-T389A-HA) were treated with 40 μM cycloheximide (MCE, CHN). Following administration of different O-GlcNAcylation regulators (50 μM PUGNAc or 50 μM OSMI-1) for 0, 12, 24 or 36 h, cell lysates were subjected to immunoblotting (IB) analysis for quantitative detection of HA-fusion protein.

sWGA pull-down assay

A succinylated wheat germ agglutinin (sWGA) pull-down assay was conducted as previously described. Briefly, preprocessed HK-2 cells and renal tissues were lysed in lysis buffer (Beyotime, CHN) supplemented with protease and phosphatase inhibitor cocktails (Thermo Fisher Scientific, USA), followed by a denaturation step in glycoprotein-denaturing buffer at 100 °C for 10 min. Then, PNGase (NEB, USA) was added to deplete N-linked glycoproteins. Afterward, the lysates were washed and incubated with prewashed sWGA biotin conjugated beads (Vector Laboratories, USA) at 4 °C overnight. Finally, the eluate containing immunoprecipitated complexes was detected by IB analysis using an anti-BACH2 antibody.

Immunoprecipitation

Preprocessed cells were scratched and lysed in precooled immunoprecipitation (IP) lysis buffer (Beyotime, CHN) supplemented with protease and phosphatase inhibitor cocktails. Next, the cleaned lysates were mixed, rotated with 2.5 μg of immunoglobulin G (IgG, CST, USA) and different target antibodies at 4 °C overnight and subsequently incubated with 30 μL of prewashed protein A/G magnetic beads (MCE, CHN) at 4 °C for 8 h. Finally, the immunoprecipitated complexes were eluted and quantitatively detected by IB analysis.

Chromatin immunoprecipitation

Cells were first rinsed with precooled PBS twice and then harvested and lysed in ice-cold lysis buffer (50 mM HEPES, 150 mM NaCl, 1 mM EDTA, 0.1% SDS, 0.1% sodium deoxycholate, 1% Triton X-100) supplemented with proteinase inhibitors for 10 min. After low-temperature centrifugation at 8000 × *g* for 5 min, the precipitate was resuspended in nuclear lysis buffer (10 mM Tris-HCl, pH: 8.0, 1 mM EDTA, and 1% SDS) containing a protease inhibitor and then sonicated to shear DNA to fragments ranging from 500 bp to 1 kb. Sonication parameter settings were as follows: output power, 60 W; open-pulse cycle, 0.5–1 s; total sonicating time, 6–8 min. Sheared chromatin was then centrifuged for 10 min at 13,000 rpm and 4 °C and transferred to a new tube for further IP. DNA fragment solution was supplemented with equal amounts of IgG or target antibody and rotated at 4 °C overnight, followed by incubation and bonding with protein A/G magnetic beads at 4 °C for 8 h. Following adequate washing, beads were soaked in DNA elution buffer and incubated at 65 °C overnight for reverse cross-linking. Then, TE buffer (10 mM Tris-HCl, 1 mM EDTA) was supplemented and administered 0.5 mg/mL RNase (Thermo Fisher Scientific, USA) at 37 °C for 30 min and 0.3 mg/mL proteinase K (Sigma–Aldrich, CHN) at 51 °C for 1 h. Finally, extractive and purified chromatin fragments were quantified by quantitative real-time PCR. The primers used for detecting SLC7A11 and GPX4 are illustrated in Supplementary File 1: Supplementary Table S1.

RNA immunoprecipitation (RIP) and MS2-RIP

The RIP assay was conducted using the Magna RIP RNA-Binding Protein Immunoprecipitation Kit (Millipore, USA) following the manufacturer's instructions. Precleaned HK-2 cells were scratched and lysed in ice-cold RIP lysis buffer and then separately incubated with 5 μg of IgG and Argonaute 2 (AGO2) antibody (Abcam, USA) on a rotator at 4 °C overnight. Afterward, protein A/G magnetic beads were added to capture the coprecipitated RNA-AGO2 complexes, and the eluate was then treated with proteinase K with shaking for protein digestion and RNA extraction. Finally, the levels of coprecipitated target RNAs were detected by quantitative real-time PCR.

An MS2-RIP assay was performed to evaluate the endogenous binding between lncRNA-WAC-AS1 and miR-449b-5p. Wild-type lncRNA-WAC-AS1 and the mutant at the miR-449b-5p binding site were separately subcloned into the plasmid pcDNA3.1-MS2 (12×) to construct pcDNA3.1-MS2-WAC-WT and pcDNA3.1-MS2-WAC-MUT plasmids. Along with the pcDNA3.1-MS2, pcDNA3.1-MS2-WAC-WT or pcDNA3.1-MS2-WAC-MUT plasmid, the pcDNA3.1-MS2/GFP plasmid encoding the MS2-GFP fusion protein was cotransfected into HK-2 cells. After 48 h, cellular RNAs were coprecipitated using GFP antibody (Abcam, USA) according to the above procedure.

Luciferase reporter assay

A luciferase reporter assay was conducted as previously described with minor modifications. 293T cells were cotransfected with pGL3-basic

plasmid containing target sequences (Supplementary File 1: Supplementary Table S2) and firefly luciferase reporter, an internal control PRL-TK plasmid, pcDNA3.1 plasmid containing cDNA encoding BACH2, or miR-449b-5p mimic (Supplementary File 1: Supplementary Table S2), and then the luciferase activity of the transfected cells was assessed through the Dual-Luciferase® Reporter Assay System (Promega, USA), with Renilla luciferase serving as the transfection control.

Quantitative real-time PCR analysis

Total RNA was extracted from sEVs, preprocessed cells or mouse tissues according to the instructions in the Takara MiniBest Universal RNA Extraction Kit (Takara, Japan). Purified total RNA was reverse transcribed utilizing a TransScript® All-in-One First-Strand cDNA Synthesis Supermix for qPCR (TransGen Biotech, CHN). Quantitative real-time PCR (qRT–PCR) was performed using a SYBR(R) Prime-Script RT–PCR kit (Takara, Japan) and an ABI 7500 sequence detection system (Applied Biosystems, USA). Each gene reaction was conducted in triplicate, and the gene expression level was determined by the internal control β-actin.

Immunoblotting

Total protein samples were obtained from cultured cells and renal tissues using radioimmunoprecipitation lysis buffer (Beyotime, CHN) supplemented with protease inhibitor (Thermo Fisher Scientific, USA). The cytoplasmic and nuclear proteins were extracted and purified by using an NE-PER Nuclear and Cytoplasmic Extraction Reagent Kit (Thermo Fisher Scientific, USA) according to the manufacturer's instructions. Immunoblotting (IB) assays were conducted as described previously [37]. Protein was separated by sodium dodecyl sulfate–polyacrylamide gel electrophoresis (SDS–PAGE), followed by blotting on polyvinylidene difluoride (PVDF) membranes (Millipore, USA). After blocking in Tris-buffered saline (TBS) containing 5% skim milk, PVDF membranes were incubated with primary antibodies at 4 °C overnight. Following washing with TBST (TBS containing Tween) three times and incubation with HRP-conjugated secondary antibody at room temperature for 1 h, protein blots were visualized with enhanced chemiluminescent substrate (Bio-Rad, USA) and quantified by ImageJ software (Supplementary Files 2 and 3).

Immunofluorescence

The cells on culture slides were fixed in 4% paraformaldehyde (Beyotime, CHN) for 10 min and permeabilized with 0.5% Triton X-100 (Thermo Fisher Scientific, USA) at room temperature for 5 min, followed by blocking with 10% normal goat serum for 1 h. After incubation with primary antibodies at 4 °C overnight and secondary antibodies at room temperature for 1 h, the slides were rinsed and mounted with antifade reagent containing DAPI for nuclear staining. Immunofluorescence (IF) images were photographed using a laser confocal microscope (Leica Microsystems AG).

Renal morphology assessment

The renal histological morphology was evaluated with hematoxylin and eosin (H&E) staining as previously described [38]. Renal tubular injury was evaluated by tubular epithelial cell swelling, tubular atrophy and dilatation, loss of brush border, vacuolization and cast formation. For statistical analysis, ten visual fields of renal tubules were randomly selected from the outer medulla of the kidney and photographed under a 400× microscope. The injury degree was reflected by pathological scoring ranging from 0 to 5 based on the percentage of injury area (0: no injury, 1: injury area < 10%, 2: 10–25%, 3: 25–50%, 4: 50–75%, 5: >75%).

Renal function assessment

The concentrations of serum creatinine (SCr) and blood urea nitrogen (BUN) were used to indicate renal function. Briefly, blood samples were collected into a heparinized Eppendorf tube and then centrifuged at 12,000 × *g* for 5 min to separate serum. The SCr and BUN in the serum samples were measured using an automated Beckman Coulter Chemistry Analyzer (Beckman Instruments, USA).

Cell viability assay

Cell viability was determined by a Cell Counting Kit 8 (CCK-8, Sigma–Aldrich, CHN) according to the manufacturer's instructions. Briefly, 5×10^3 HK-2 cells per well were inoculated into a 96-well plate 24 h prior to further administration. Then, 10 μL of CCK-8 reagent was added to the wells and incubated at 37 °C for 1 h. The absorbance was measured at 450 nm using a microplate reader (Bio-Rad, USA).

Lipid peroxidation assay

The malondialdehyde (MDA) concentrations in cells and tissues were quantified by using a lipid peroxidation assay kit (Abcam, UK). In short, TBA reagent was incubated with standards and samples at 95 °C for 1 h and then cooled to room temperature in an ice bath for 10 min. Finally, 200 μL of the reaction mixture was transferred into a 96-well plate for absorbance measurement at 532 nm using a microplate reader (Bio-Rad, USA).

Glutathione assay

The glutathione (GSH) concentration was detected using a commercial Glutathione Assay Kit (Elabscience, CHN). To minimize autoxidation and degradation of GSH, 5% 5-sulfosalicylic acid solution was used to prepare cell and tissue samples. Next, 10 μL of lysate supernatant was added into a 96-well plate and incubated with reaction mix at room temperature for 5 min. The GSH content was determined by measuring absorbance in a kinetic manner at a wavelength of 405 nm and normalized by the standard.

Iron assay

The relative iron levels in cells or tissues were assessed using an Iron Assay kit (Elabscience, CHN). Cell and tissue samples were homogenized in ice-cold iron assay buffer, followed by low-temperature centrifugation at 16,000 × *g* for 10 min. Then, 10 μL of supernatant was transferred into a 96-well plate, and the volume was brought to 100 μL with supplementation of iron assay buffer. Afterward, iron reducer (5 μL) was added to each mixture, which was incubated at 25 °C for 30 min. Following further dark incubation with iron probe, the absorbance was measured at a wavelength of 593 nm using a microplate reader (Bio-Rad, USA).

Statistical analysis

GraphPad Prism 5 (GraphPad software, USA) and Statistical Product and Service Solutions (SPSS, IBM, USA) were utilized for statistical analyses. Sample sizes were based in standard protocols in the field, and the sample size of each experiment was indicated in figure legend. Data were presented as the mean ± SD from at least three independent experiments for each group. The investigators were blinded to the group allocation during the experiment and data collection. Unpaired or paired 2-tailed Student's *t* test was used to compare the statistical significance between the two groups. One-way ANOVA followed by Tukey's multiple comparisons test was utilized for multigroup comparisons. Pearson's correlation coefficient was employed to determine linear correlations. Before assumptions for these tests, sample independence, normal distribution, and variance equality were assumed to be met. Statistical significance was defined as $p < 0.05$. $^*p < 0.05$, $^{**}p < 0.01$, $^{***}p < 0.001$.

RESULTS

IRI-sEVs facilitate ferroptosis propagation among normal renal tubular epithelial cells

To determine whether IRI cell-secreted sEVs (IRI-sEVs) mediate ferroptosis propagation, we used 47 pairs of usEVs derived from 29 donors before KT (preKT-dusEVs) and 47 recipients 24/48 h after KT (postKT-rusEVs-24/48 h) to treat normal HK-2 cells (Fig. 1A and Supplementary File 1: Supplementary Fig. S1A–D). We detected that postKT-rusEVs prominently promoted ferroptosis in HK-2 cells, as evidenced by the higher levels of lipid peroxidation and iron and the reductions in GSH and cell viability (Fig. 1B–E). In addition, HK-2 cell-derived sEVs validated that IRI-sEVs (postIR-csEVs-24/48 h) induced ferroptosis spread among normal HK-2 cells (Supplementary File 1: Supplementary Fig. S1E–K). To gain further unambiguous insights into the indispensable effect of sEVs on ferroptosis spread, we used different HK-2 cell conditioned medium (CM) to incubate normal HK-2 cells to simulate the renal tissue microenvironment (Supplementary File 1: Supplementary Fig. S1L). As illustrated in

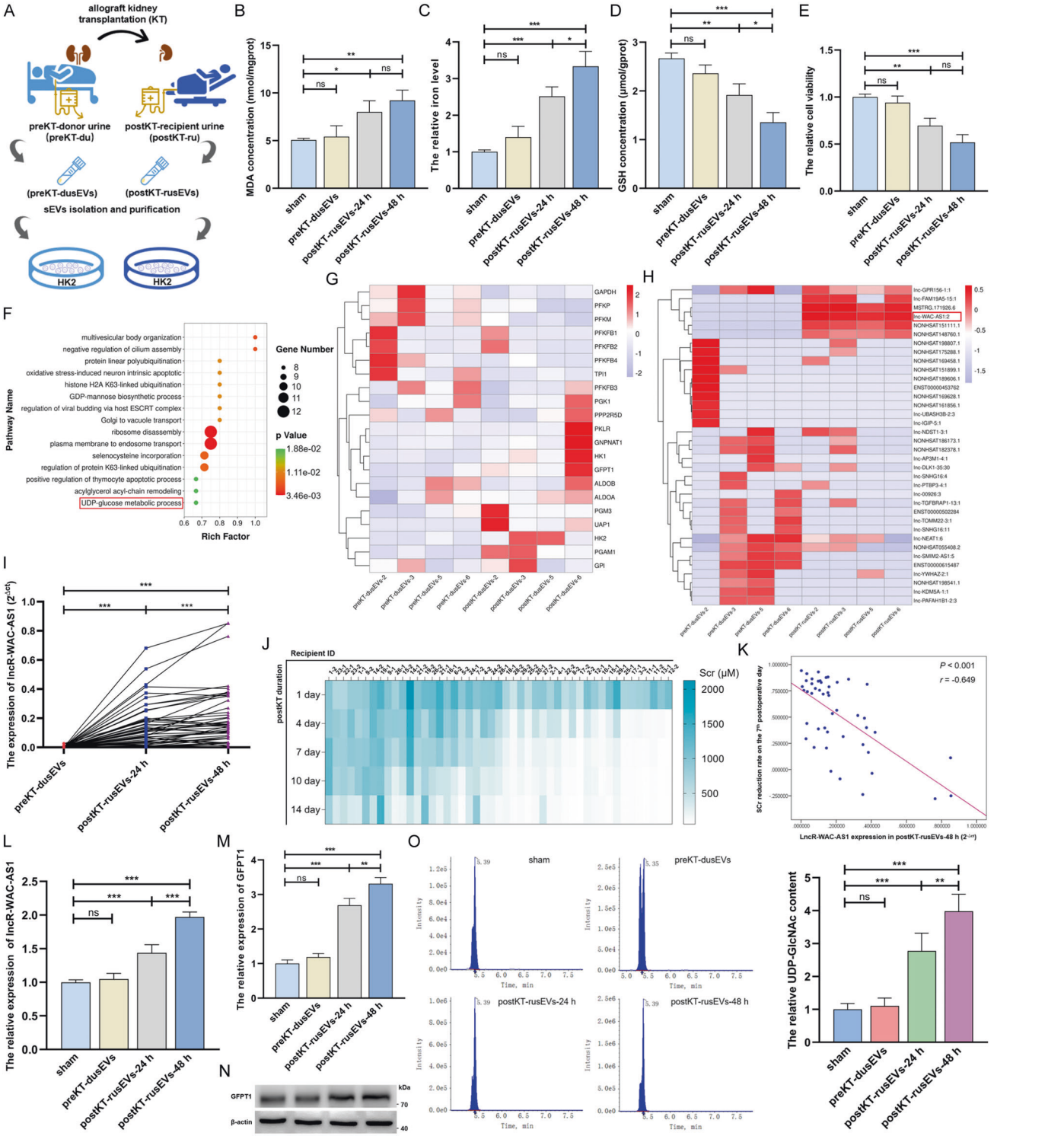

Supplementary File 1: Supplementary Fig. S1M–P, the CM of IRI HK-2 cells (postIR-CM) caused prominent increases in lipid peroxidation and iron levels and downregulation of GSH and cell viability in normal HK-2 cells, while these alterations were significantly blunted when the biogenesis and secretion of EVs was inhibited by GW4869 or when EVs were eliminated from CM. These data obtained in patient and cell specimens confirm the crucial role of IRI-sEVs in promoting "wave of ferroptosis" propagation.

LncRNA-WAC-AS1 enriched in IRI-sEVs promotes HBP metabolic reprogramming by upregulating GFPT1 in normal renal tubular epithelial cells

We next performed whole transcriptome sequencing analysis using four pairs of preKT-dusEVs and postKT-rusEVs to ascertain the cargo variation in sEVs induced by renal IRI (Supplementary File 1: Supplementary Fig. S2A) and found that lncRNAs upregulated in postKT-rusEVs were mainly enriched for metabolic processes (Supplementary File 1: Supplementary Fig. S2B) and

Fig. 1 IRI-sEVs foster ferroptosis and HBP metabolism in normal renal tubular epithelial cells. A Flowchart delineating the process of the in vitro intervention model established by HK-2 cells and usEVs derived from the paired donor and recipient. **B**–**E** MDA concentration, iron level, GSH concentration and cell viability were measured in HK-2 cells before and after 47 pairs of usEV treatments; the iron level and cell viability were normalized according to the result of sham; one-way ANOVA followed by Tukey's test. **F** Gene Ontology analysis of upregulated lncRNAs in postKT-rusEVs. **G** Target gene predictive analysis of identified differential lncRNAs in preKT-dusEVs and postKT-rusEVs. **H** Cluster heatmap illustrating the differential glucose metabolism-related lncRNAs between the paired preKT-dusEVs ($n = 4$) and postKT-rusEVs ($n = 4$). **I** The level of lncRNA-WAC-AS1 in the paired preKT-dusEVs ($n = 29$), postKT-rusEVs-24 h ($n = 47$) and postKT-rusEVs-48 h ($n = 47$) was measured by qRT–PCR and quantitatively analyzed by paired 2-tailed Student's t test. **J** Heatmap showing the SCr concentration of recipients after kidney transplantation. **K** Correlation analysis between lncR-WAC-AS1 level in postKT-rusEVs-48 h and SCr recovery rate on the 7th postoperative day ($n = 47$). The relative lncRNA-WAC-AS1 level (**L**) and the transcriptional (**M**) and translational (**N**) levels of GFPT1 (the crucial rate-limiting enzyme in the HBP) in HK-2 cells following 47 pairs of usEV treatments; one-way ANOVA followed by Tukey's test. **O** The relative level of UDP-GlcNAc in HK-2 cells before and after 47 pairs of usEV treatments (left) and quantitative analysis (right); metabolite content was normalized according to the level of sham; one-way ANOVA followed by Tukey's test. ***$p < 0.001$, **$p < 0.01$, and *$p < 0.05$ represent significant differences between two groups; ns represents no significant difference.

UDP-glucose metabolic processes (Fig. 1F). Target gene predictive analysis of differential lncRNAs implied that glucose metabolic enzymes were prominently altered, of which GFPT1 was notably increased in postKT-rusEVs (Fig. 1G). Targeted screening identified lncRNA-WAC-AS1 as one of the glucose metabolism-related lncRNAs that was strikingly increased in postKT-rusEVs (Fig. 1H), which was further corroborated in 47 pairs of usEVs (Fig. 1I and Supplementary File 1: Supplementary Fig. S2C). In addition, Pearson correlation analysis illuminated that the level of lncRNA-WAC-AS1 in postKT-rusEVs, rather than preKT-dusEVs, was inversely correlated with the graft function recovery rate, such as SCr ($r = -0.649$, $p < 0.001$, $n = 47$, Fig. 1J, K and Supplementary File 1: Supplementary Fig. S2D) and BUN ($r = -0.615$, $p < 0.001$, $n = 47$, Supplementary File 1: Supplementary Fig. S2E–G), indicating that lncRNA-WAC-AS1 could be a potential biomarker for predicting and evaluating graft function recovery.

Then, we tested whether IRI-sEVs regulate glucose metabolism in normal HK-2 cells and detected a striking increase in lncRNA-WAC-AS1 in HK-2 cells following postKT-rusEV treatment (Fig. 1L). Moreover, the transcriptional and translational levels of GFPT1 (Fig. 1M, N and Supplementary File 2) were also upregulated, accompanied by an increase in UDP-GlcNAc (Fig. 1O). Interestingly, other metabolic enzymes (Supplementary File 1: Supplementary Fig. S3A–E) and metabolites (Supplementary File 1: Supplementary Fig. S3F) in glucose metabolism and the HBP branch were almost constant. Analogously, the crucial rate-limiting enzyme and end metabolite in the HBP as well as lncRNA-WAC-AS1 were all increased following treatment with postIR-csEVs containing an overwhelming amount of lncRNA-WAC-AS1 but had no impact on other glucose metabolic enzymes, suggesting that IRI-sEVs upregulate GFPT1 and increase HBP metabolic fluxes (Supplementary File 1: Supplementary Fig. S4A–I and Supplementary File 2: Supplementary Fig. S4D).

To gain further unambiguous insights into the predominant effect of lncRNA-WAC-AS1 on facilitating HBP metabolism, we established IRI models in lncRNA-WAC-AS1-overexpressing and -knockout HK-2 cell lines and isolated sEVs to treat normal HK-2 cells (Supplementary File 1: Supplementary Fig. S5A, B). Under this condition, the level of lncRNA-WAC-AS1 in normal HK-2 cells was altered contextually to the changes in exogenous supplementation of IRI-sEVs (Supplementary File 1: Supplementary Fig. S5C). In addition, the alterations in GFPT1 and UDP-GlcNAc were in trajectory parallel to that of lncRNA-WAC-AS1 (Supplementary File 1: Supplementary Fig. S5D, F and Supplementary File 2: Supplementary Fig. S5E). Consistent with the observations after postKT-rusEV and postIR-csEV treatments, lncRNA-WAC-AS1 did not affect other glucose metabolic enzymes, such as HK II, GNA1, PGM3 or UAP1 (Supplementary File 1: Supplementary Fig. S5G–J). Besides, the addition of IRI-sEVs delivering different lncRNA-WAC-AS1 levels showed scarcely any effects on the key enzymes (PFKM and PKM) in glycolysis pathway (Supplementary File 1: Supplementary Fig. S5K–L). Based on these findings, we deduce that lncRNA-WAC-AS1 enriched in IRI-sEVs increases HBP metabolic fluxes by upregulating GFPT1 in normal HK-2 cells, thereby promoting HBP metabolic reprogramming.

LncRNA-WAC-AS1 promotes GFPT1 expression via sequestration of miR-449b-5p

GFPT1 is a pivotal switch regulating HBP metabolic flux branched off from glycolysis, but how it is induced by lncRNA-WAC-AS1 remains to be further dissected. In a set of miRNAs that are putatively bound to lncRNA-WAC-AS1 and GFPT1 in the starBase database (https://starbase.sysu.edu.cn, Supplementary File 1: Supplementary Fig. S6A), we focused on two metabolism-related miRNAs, miR-369-3p and miR-449b-5p. Further validation indicated that miR-449b-5p was deemed a potential mediator in lncRNA-WAC-AS1-induced GFPT1 upregulation, since lncRNA-WAC-AS1 decreased the level of miR-449b-5p, which had an inhibitory effect on GFPT1 expression (Fig. 2A–C and Supplementary File 1: Supplementary Fig. S6B, C). To ascertain the interaction between lncRNA-WAC-AS1 and miR-449b-5p, we performed dual luciferase assays with reporters bearing lncRNA-WAC-AS1 parental cDNA or the mutant at the putative miR-449b-5p-binding site (only one binding site in the starBase database), and the results showed that the luciferase activity of lncRNA-WAC-AS1-WT, but not MUT, was sharply attenuated by miR-449b-5p (Fig. 2D). Besides, we detected that the level of lncRNA-WAC-AS1 was significantly higher than that of miR-449b-5p in HK-2 cells, which further implies the effectiveness of lncRNA-WAC-AS1, functioning as a competing endogenous RNA, on binding to miR-449b-5p (Supplementary File 1: Supplementary Fig. S6D). It has been well documented that the interaction between lncRNA and miRNA relies on an AGO2 complex; therefore, an AGO2-RIP assay was conducted and found that lncRNA-WAC-AS1 was directly bound to the AGO2-containing miR-449b-5p ribonucleoprotein complex, but the interaction was sharply reduced upon inhibition of miR-449b-5p (Fig. 2E). In addition, the MS2-RIP assay showed that endogenous miR-449b-5p was pulled down by the MS2-lncRNA-WAC-AS1-WT complex, further corroborating the endogenous binding capacity of lncRNA-WAC-AS1 with miR-449b-5p (Fig. 2F, G).

Next, the interaction between miR-449b-5p and GFPT1 was verified by dual luciferase assays, illustrating that miR-449b-5p mimics prominently reduced the luciferase activity of the GFPT1 reporter (Fig. 2H). Due to the above data showing that lncRNA-WAC-AS1 shares miR-449b-5p with the 3′ UTR of GFPT1, we therefore sought to explore whether miR-449b-5p modulates lncRNA-WAC-AS1-mediated GFPT1 upregulation. After introducing the miR-449b-5p mimic and inhibitor into WOE and WKO cells, respectively, lncRNA-WAC-AS1-induced GFPT1 elevation was strikingly reversed by the miR-449b-5p mimic (Fig. 2I); in contrast, the addition of the miR-449b-5p inhibitor increased the GFPT1 level, which was downregulated following lncRNA-WAC-AS1 knockout (Fig. 2J). These collective results suggest that lncRNA-

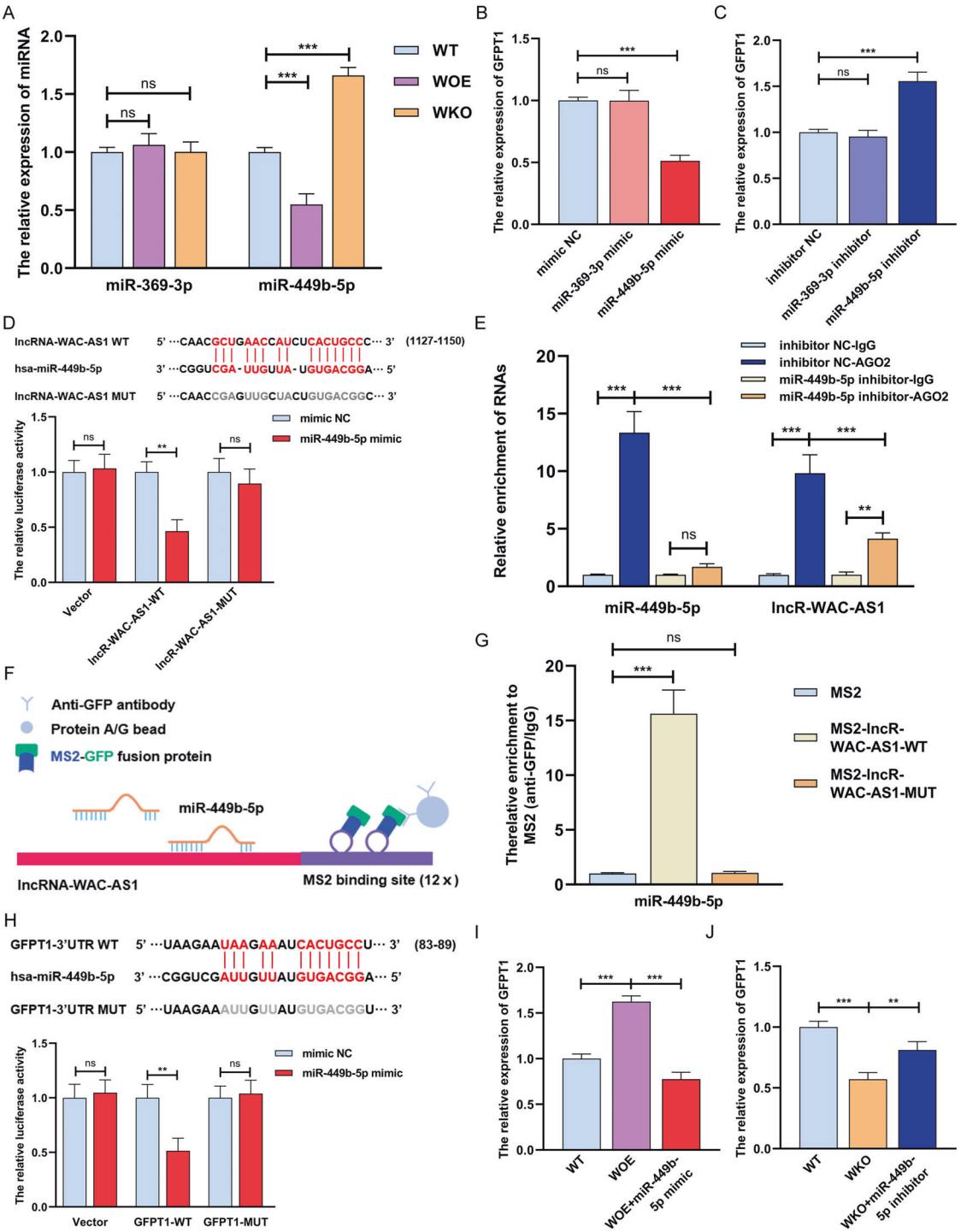

WAC-AS1 promotes GFPT1 expression by competitively binding to and inhibiting miR-449b-5p.

HBP metabolic acceleration facilitates ferroptosis by inhibiting SLC7A11 and GPX4

The distinct key roles of glucose-related metabolic pathways, including glycolysis, PPP, OXPHOS and the TCA cycle, in ferroptosis have gradually become understood. However, it remains unclear whether and how glucose-related HBP metabolism modulates ferroptosis. To test this possibility, we generated GFPT1 global knockout (GFKO) mice in which HBP metabolism was impeded and established an in situ kidney IRI model in wild-type (WT) and GFKO mice (Fig. 3A). We first validated these IRI models by glucose metabolic profiling of renal tissues, in which UDP-GlcNAc was considerably induced by IRI but sharply decreased in GFKO mice (Fig. 3B, C). In addition, IRI prominently increased the levels of GFPT1 and O-GlcNAc posttranslational modification in renal tissues of WT mice (Fig. 3D and Supplementary File 2) and simultaneously provoked renal impairments in morphology and function, as evidenced by the notable increase in tubular injury area (Fig. 3E) and the SCr and BUN concentrations (Fig. 3F, G). However, renal injury was dramatically reversed in

Fig. 2 LncRNA-WAC-AS1 functions as a competing endogenous RNA by directly binding to miR-449b-5p and facilitates GFPT1 expression. A The relative levels of miRNAs in different HK-2 cell lines ($n = 6$ group^{-1}); the results were normalized according to miRNA levels in WT; one-way ANOVA followed by Tukey's test. qRT–PCR measuring the relative expression of GFPT1 in HK-2 cells transfected with miRNA mimics (**B**) and inhibitors (**C**); the results were normalized according to GFPT1 expression in mimic NC or inhibitor NC; one-way ANOVA followed by Tukey's test. **D** Parental (WT) and mutant lncRNA-WAC-AS1 sequences were cloned into pGL3-basic plasmid and co-transfected with miR-449b-5p into 293T cells followed by dual luciferase assays ($n = 3$ group^{-1}); the results were normalized according to the luciferase activity in 293T cells transfected with mimic NC; unpaired 2-tailed Student's *t* test. **E** RIP assays were utilized to pulldown the endogenous RNA associated with AGO2 in HK-2 cells transfected with miR-449b-5p inhibitor or inhibitor NC, and the relative levels of lncRNA-WAC-AS1 and miR-449b-5p were measured and normalized according to the result in IgG group ($n = 3$ group^{-1}); one-way ANOVA followed by Tukey's test. **F** Schematic delineating the strategy of MS2-RIP. **G** MS2-RIP assays in HK-2 cells followed by qRT–PCR examining the endogenous binding between lncRNA-WAC-AS1 and miR-449b-5p ($n = 3$ group^{-1}); the results were normalized according to the miR-449b-5p level in MS2 group; one-way ANOVA followed by Tukey's test. **H** Parental and mutant GFPT1 sequences (top) and the luciferase activity in 293T cells (bottom, $n = 3$ group^{-1}); the results were normalized according to the mimic NC group; unpaired 2-tailed Student's *t* test. **I, J** The results of qRT–PCR showing the relative levels of GFPT1 in distinct HK-2 cells following different treatments ($n = 6$ group^{-1}); the expression levels were normalized according to the result in WT HK-2 cells; one-way ANOVA followed by Tukey's test. ***$p < 0.001$ and **$p < 0.01$ represent significant differences between two groups; ns represents no significant difference.

GFKO mice, accompanied by the downregulation of GFPT1 and O-GlcNAcylation. These findings imply that HBP metabolic acceleration aggravates renal IRI. Intriguingly, we isolated and purified tsEVs in the renal tissue microenvironment and detected that the level of lncRNA-WAC-AS1 in renal tsEVs was markedly elevated in WT mice after IRI but diminished to some extent in GFKO mice, probably because of the mitigation of renal IRI (Fig. 3H).

To decipher the association between HBP metabolism and ferroptosis, we detected that the levels of lipid peroxidation and iron and the decrease in GSH concentration were enhanced in renal tissues of WT-IR mice, indicating the upregulation of ferroptosis, whereas GFKO-IR mice illustrated the opposite results (Fig. 3I–K). After examining ferroptosis-related genes, we unexpectedly found that the transcriptional and translational levels of SLC7A11 and GPX4, which are pivotal genes in the cyst(e)ine/GSH/GPX4 antioxidant system, were strikingly decreased during IRI but dramatically upregulated in the renal tissues of GFKO mice (Fig. 3L–N and Supplementary File 2: Fig. 3N). Importantly, the results of IF showed that the IRI-induced reduction in SLC7A11 was lumped and regional, and knockout of GFPT1 partially reversed the downregulation (Fig. 3O). Therefore, we speculate that diminishing HBP flux by targeted knockout of GFPT1 could facilitate SLC7A11 and GPX4 expression, consequently heightening cellular antioxidant capacity and inhibiting ferroptosis propagation through adjacent cell populations. To substantiate this deduction, we first ascertained that the addition of IRI-sEVs indeed caused notable suppression of SLC7A11 and GPX4 at both the transcriptional and translational levels in normal HK-2 cells (Supplementary File 1: Supplementary Fig. S7A–F and Supplementary File 2: Supplementary Fig. S7C, F), which was consistent with the ferroptosis alteration (Fig. 1B–E and Supplementary File 1: Supplementary Fig. S1F–I). Taken together, these findings provide compelling evidence that GFPT1 overexpression-induced HBP metabolic acceleration suppresses SLC7A11 and GPX4 expression, thus facilitating ferroptosis.

Knockout of GFPT1 suppresses BACH2 O-GlcNAcylation at Thr389 induced by IRI

One of the most important functions of HBP metabolism is to fuel O-GlcNAc posttranslational modification by synthesizing UDP-GlcNAc. We wondered if protein O-GlcNAcylation participates in HBP metabolic reprogramming-mediated inhibition of SLC7A11 and GPX4 and promotion of ferroptosis. We therefore performed O-GlcNAcylation omics analysis to identify differentially O-GlcNAcylated proteins in mouse renal tissues (Fig. 4A). Finally, 435 O-GlcNAcylated proteins and 1214 O-GlcNAcylated sites were quantified, and there were 188 and 116 O-GlcNAcylated differential proteins in the comparisons of WT-sham vs. WT-IR and WT-IR vs. GFKO-IR, respectively (Fig. 4B), of which the O-GlcNAc modification of BACH2 at the threonine 389 residue (Thr389), a transcription repressor participating in cellular oxidative regulation, showed notable differences in both comparisons and sparked our interest (Fig. 4C). Indeed, sWGA pull-down assays corroborated that the levels of O-GlcNAcylated BACH2 were considerably elevated after renal IRI but sharply reversed in GFKO mice (Fig. 4D).

In addition, the interaction between BACH2 and OGT, at exogenous and endogenous levels, was confirmed by co-IP assays in 293T cells and HK-2 cells, respectively (Fig. 4E–G). Furthermore, we dissected the precise interacting domain(s) of BACH2 with OGT by constructing different HA-tagged fragments of BACH2 and found that the heme-binding domain (HBD) is required for interacting with OGT (Supplementary File 1: Supplementary Fig. S8A, B). BACH2 O-GlcNAcylation was further validated by an evident interaction between BACH2 and O-GlcNAc in HK-2 cells (Supplementary File 1: Supplementary Fig. S8C) and 293T cells (Supplementary File 1: Supplementary Fig. S8D). In addition, the O-GlcNAc modification of BACH2 was significantly elevated when O-GlcNAcase (OGA) was inhibited by PUGNAc, but was reversely suppressed by OSMI-1 (an OGT inhibitor) (Supplementary File 1: Supplementary Fig. S8E). Next, we determined the O-GlcNAcylated sites via site-directed mutagenesis using alanine to replace four identified O-GlcNAcylated sites (T360A, T389A, T442A and T520A). Consistent with the results of MS analysis, the mutant on Thr 389 evoked the most dramatic reduction in the O-GlcNAcylated level, indicating that Thr 389 is the key O-GlcNAcylated site on BACH2 (Supplementary File 1: Supplementary Fig. S8F). These findings collectively imply that GFPT1 upregulation-induced HBP metabolic acceleration facilitates BACH2 O-GlcNAcylation at Thr389 in the renal IRI process.

IRI-sEVs delivering lncR-WAC-AS1 promote BACH2 O-GlcNAcylation and thus increase the stability and nuclear translocation of BACH2 in normal renal tubular epithelial cells

Next, we focused on O-GlcNAcylation-mediated functional alterations in BACH2. The results of cycloheximide-chase assays suggested that inhibition of O-GlcNAcylation with OSMI-1 sharply shortened the half-life of parental BACH2, which was prolonged in WOE cells (Fig. 5A, B) but showed a weaker effect on the T389A mutant (Fig. 5C, D), implying that lncRNA-WAC-AS1-induced BACH2 O-GlcNAcylation at Thr389 prominently increased the stability of BACH2. We subsequently identified that enhancing O-GlcNAcylation reduced the interaction between BACH2-WT and Ub and accordingly inhibited proteasome-mediated degradation, but OSMI-1 reversely provoked a considerable increase in the interaction between BACH2-WT and Ub in WOE cells (Fig. 5E). In contrast, the regulatory roles of PUGNAc and OSMI-1 were evidently blunted when the Thr389 residue was mutated to alanine (Fig. 5F). Together with these findings, we propose a new

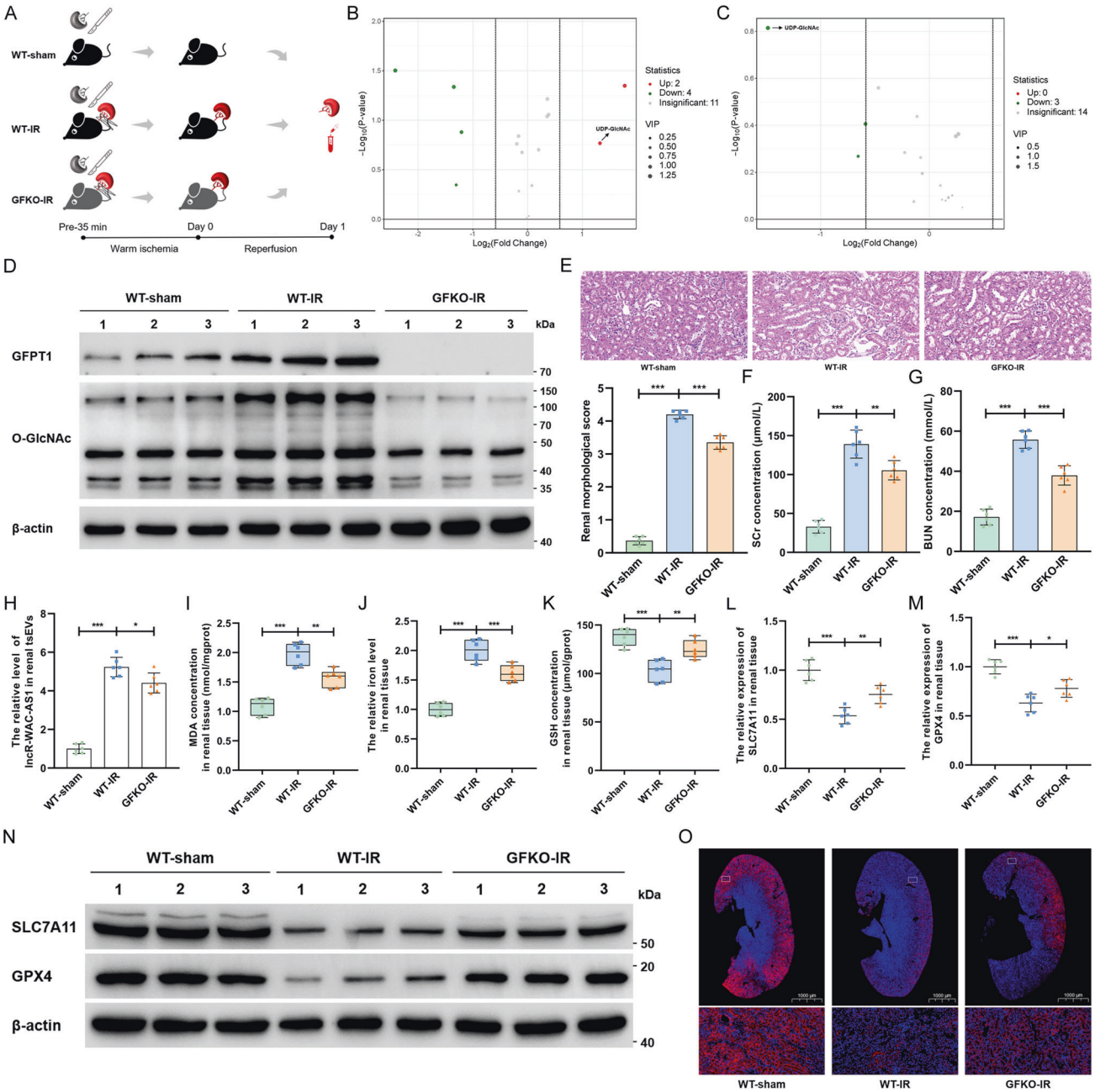

Fig. 3 GFPT1-mediated HBP metabolic acceleration suppresses SLC7A11 and GPX4 expression and promotes ferroptosis in mouse renal IRI model. A Schematic representing in situ kidney warm ischemia-reperfusion injury protocol in WT and GFPT1 global knockout C57BL/6 mice. **B** Volcano plot illustrated all detected glucose metabolism-related metabolites in renal tissues of mice in WT-sham and WT-IR groups ($n = 6$ group^{-1}). The red dots represent the prominently upregulated metabolites in the WT-IR group; green dots represent the considerably downregulated metabolites, and gray dots indicate no significant differences. **C** Volcano plot showing all detected glucose metabolites in WT-IR and GFKO-IR groups ($n = 6$ group^{-1}). The green dots represent the significantly downregulated metabolites in GFKO-IR group. **D** IB assays examined the expression of GFPT1 and O-GlcNAc in renal tissues of WT and GFKO mice before and after IRI treatment. **E** HE staining (top) and renal pathological score (bottom) of renal tissue slice ($n = 6$ group^{-1}); scale bar: 20 μm; one-way ANOVA followed by Tukey's test. The SCr (**F**) and BUN (**G**) concentrations of mice following different administrations ($n = 6$ group^{-1}); one-way ANOVA followed by Tukey's test. **H** The lncRNA-WAC-AS1 level in renal-derived tsEVs was normalized according to the level of WT-sham ($n = 6$ group^{-1}); one-way ANOVA followed by Tukey's test. MDA concentration (**I**), iron level (**J**) and GSH concentration (**K**) in renal tissues were normalized according to the level of WT-sham ($n = 6$ group^{-1}); one-way ANOVA followed by Tukey's test. The transcriptional (**L**, **M**) and translational (**N**) levels of SLC7A11 and GPX4 in renal tissues ($n = 6$ group^{-1}); one-way ANOVA followed by Tukey's test. **O** IF assays determining the expression level and region of SLC7A11 (red) in renal tissue slices; scale bar: 1000 μm for the 1X and 20 μm for the 400X. ***$p < 0.001$, **$p < 0.01$, and *$p < 0.05$ represent significant differences between two groups.

mechanism by which BACH2 O-GlcNAcylation at Thr389 enhances protein stability by inhibiting ubiquitination.

We have provided a solid basis that GFPT1 overexpression-induced HBP metabolic reprogramming facilitates O-GlcNAc modification of BACH2 and thus increases protein stability. Next, we further ascertained whether lncRNA-WAC-AS1 drives the foregoing regulatory program in HK-2 cells. Indeed, altering endogenous lncRNA-WAC-AS1 did not affect the transcriptional

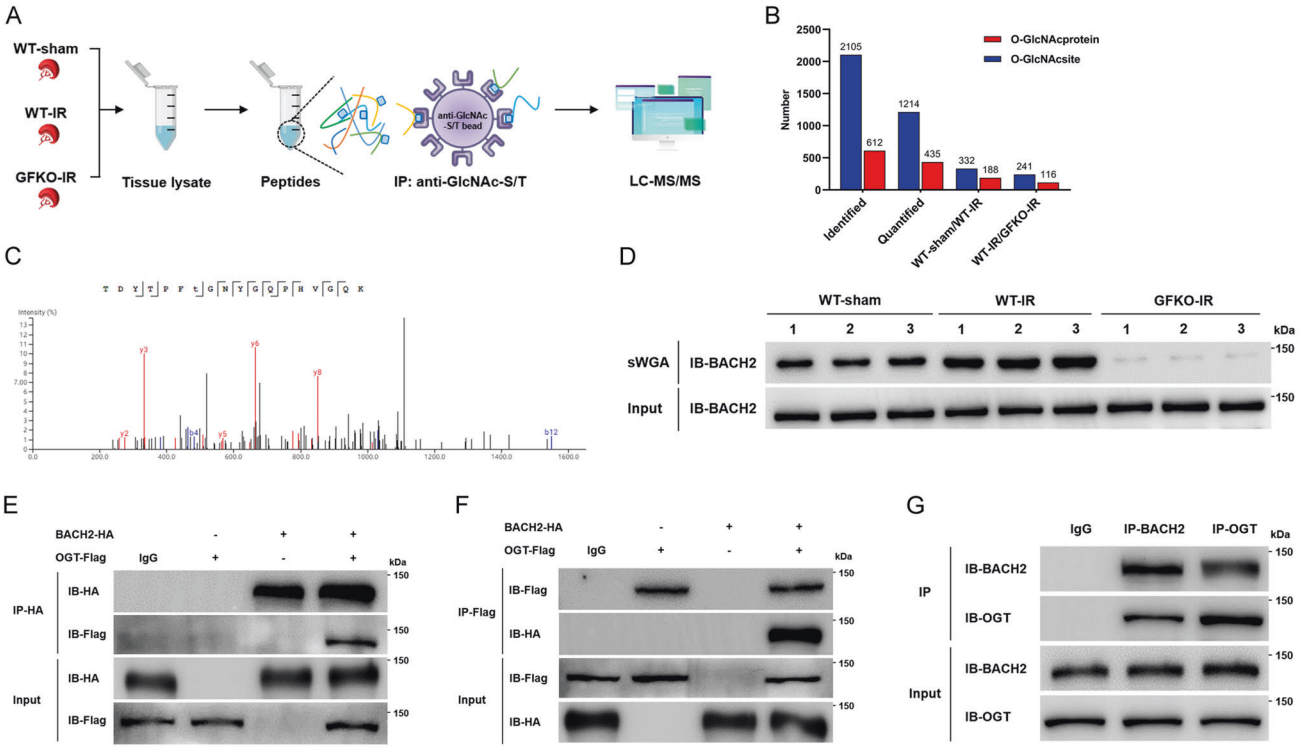

Fig. 4 GFPT1-induced HBP metabolic acceleration fosters BACH2 O-GlcNAcylation in renal IRI process. A, **B** Schematic delineating the flows and results of O-GlcNAcylation LC-MS/MS analysis of mouse renal tissues ($n = 3$ group^{-1}). **C** MS analysis identified residue Thr389 as the BACH2 O-GlcNAcylated site. **D** sWGA pull-down assays were conducted in mouse renal tissues ($n = 6$ group^{-1}); IB assays were determined using anti-BACH2. Co-IP assays of BACH2-HA and OGT-Flag were examined using an anti-HA antibody (**E**) or an anti-Flag antibody (**F**) in 293 T cells. **G** Co-IP assays of the endogenous BACH2 and OGT in HK-2 cells.

level of BACH2 (Fig. 5G) but caused a dramatic upregulation at the protein level (Fig. 5H and Supplementary File 2). Consistently, IRI-sEV-mediated exogenous lncRNA-WAC-AS1 alterations only drove the translational levels of BACH2, showing scarcely any effects on the mRNA level (Fig. 5I, J and Supplementary File 2). The findings were further corroborated in clinical kidney transplant samples (Fig. 5K, L and Supplementary File 2). Therefore, we conclude that IRI-sEVs delivering lncRNA-WAC-AS1 enhance the protein stability and global protein level of BACH2 by promoting HBP metabolism-mediated BACH2 O-GlcNAcylation in normal renal tubular epithelial cell populations.

It has been documented that the regulatory functions of BACH2 mainly rely on nuclear localization, and a growing body of mechanisms have been elucidated that modulate BACH2 nuclear translocation, including diverse posttranslational modifications [39–41]. Therefore, we wondered whether and how O-GlcNAc modification affects the subcellular localization of BACH2. Unexpectedly, the IF assay illustrated that the addition of PUGNAc strikingly elevated the global levels of BACH2, especially in the nucleus, while suppression of O-GlcNAcylation dramatically reversed the increased nuclear localization of BACH2 (Fig. 5M). Of special importance, we unequivocally observed that O-GlcNAcylated BACH2 was predominantly located in the nucleus after PUGNAc administration (Fig. 5M). IB assays further corroborated that in the absence of proteasome-mediated degradation, PUGNAc treatment provoked the intranuclear accumulation of BACH2, whereas OSMI-1 had the opposite effect (Fig. 5N and Supplementary File 2). In addition, postIR-csEVs-48 h delivering lncRNA-WAC-AS1 increased the endogenous BACH2 level in the nucleus (Supplementary Files 1 and 2, Supplementary Fig. S9A). Previous studies have revealed that BACH2 possesses a nuclear localization signal (NLS) in the basic domain [39, 42]; therefore, we attempted to investigate whether importin α5, a nuclear adaptor binding specifically and directly to the NLS motif, modulates the nuclear import of BACH2. Indeed, the elevation of O-GlcNAcylation in WOE cells or PUGNAc-treated WT cells led to a considerably increased interaction between importin α5 and BACH2 but dropped after administration of OSMI-1 (Supplementary Files 1 and 2, Supplementary Fig. S9B). More persuasively, we detected that the BACH2 level in the nucleus was sharply reduced when the encoding gene of importin α5 was silenced by siRNA, accordingly aggravating the accumulation of cytoplasmic BACH2 (Supplementary File 1, Supplementary Fig. S9C). These results, from another prospective, reveal that lncRNA-WAC-AS1-strengthened O-GlcNAcylation regulates the function of BACH2 by facilitating importin α5-mediated nuclear translocation.

BACH2 O-GlcNAcylation facilitates ferroptosis by potentiating BACH2-mediated transcriptional suppression of SLC7A11 and GPX4

In light of our finding that HBP metabolic acceleration promotes ferroptosis by inhibiting SLC7A11 and GPX4 expression, we next sought to examine whether HBP metabolism-induced O-GlcNAc modification of BACH2, acting as a transcription repressor, mediates the transcriptional suppression of SLC7A11 and GPX4, accordingly inducing ferroptosis. We first determined the pivotal role of BACH2 in promoting ferroptosis by using erastin (a ferroptosis inducer) and ferrostatin-1 (a ferroptosis inhibitor). As illustrated in Supplementary File 1: Supplementary Fig. S10A–D, siRNA-BACH2 showed an unequivocally reversing effect on erastin-induced ferroptosis, as evidenced by the reductions in lipid peroxidation and iron levels and boosts in GSH concentration and cell viability. Reciprocally, ferroptosis was sharply elevated in BACH2-overexpressing HK-2 cells (BOE) but decreased to some extent after ferrostatin-1 treatment. Then, we tested whether O-GlcNAcylated BACH2 facilitates ferroptosis by

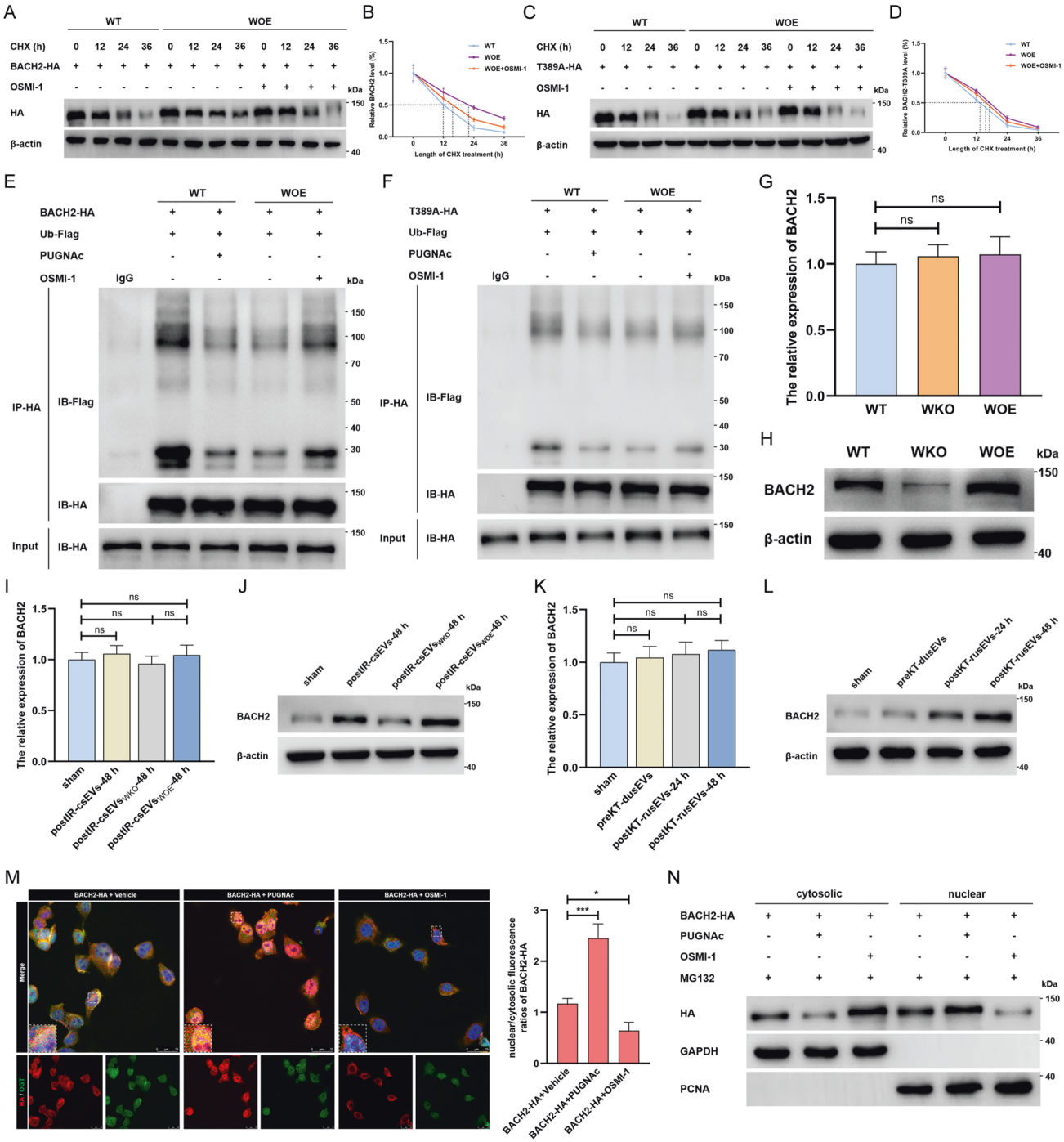

Fig. 5 LncRNA-WAC-AS1-faciliated BACH2 O-GlcNAcylation enhances protein stability and nuclear translocation of BACH2. A Protein stability detection and half-life analysis of parental BACH2-HA (**A**, **B**) and BACH2-Thr389A-HA mutant (**C**, **D**) in WT HK-2 cells and WOE HK-2 cells treated with vehicle or 50 μM OSMI-1. The ubiquitination assays of the parental BACH2 (**E**) and BACH2-Thr389A mutant (**F**) in WT and WOE HK-2 cells co-transfected with Flag-tagged ubiquitin (Ub-Flag). The transcriptional (**G**) and translational (**H**) levels of BACH2 in HK-2 cells with different endogenous lncRNA-WAC-AS1 expression ($n = 6$ group^{-1}); one-way ANOVA followed by Tukey's test. **I**–**L** The expression of BACH2 in normal HK-2 cells after treatments with IRI-sEVs containing distinct levels of the exogenous lncRNA-WAC-AS1; one-way ANOVA followed by Tukey's test. **M** IF (left) and quantitative assays (right) showing the expression, subcellular localization and colocalization of BACH2-HA (red) and OGT (green) in HK-2 cells transfected with BACH2-HA following administration of vehicle, 50 μM PUGNAc or 50 μM OSMI-1; scale bar: 25 μm. **N** IB results illustrating the cytosolic and nuclear levels of HA-tagged BACH2 in HK-2 cells treated with 40 μM MG132 and 50 μM PUGNAc either or 50 μM OSMI-1. ***$p < 0.001$ and *$p < 0.05$ represent significant differences between two groups; ns represents no significant difference.

inhibiting SLC7A11 and GPX4. We detected that overexpression of BACH2 indeed led to a prominent reduction in SLC7A11 and GPX4 at the transcriptional level (Supplementary File 1: Supplementary Fig. S10E–G) and translation level (Supplementary Files 1 and 2: Supplementary Fig. S10H), accompanied by higher levels of lipid peroxidation and iron and decreases in GSH and cell viability (Supplementary File 1: Supplementary Fig. S10I–L). Importantly, the induction of ferroptosis and the inhibition of SLC7A11 and

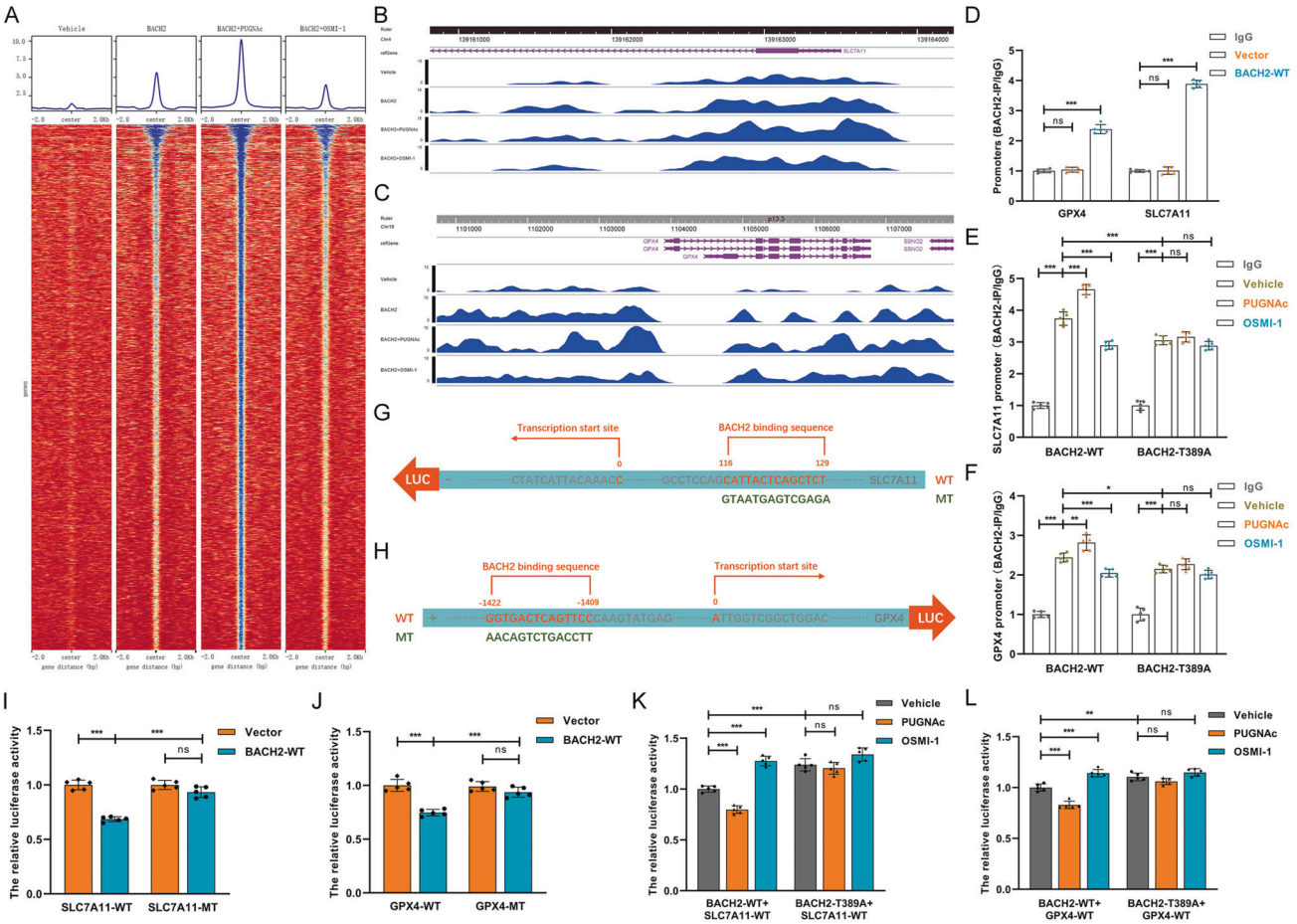

Fig. 6 BACH2 O-GlcNAcylation strengthens BACH2-mediated transcriptional suppression to SLC7A11 and GPX4. A ChIP–seq analysis was performed and genome-wide binding sites of BACH2 were mapped in HK-2 cells following treatments with vehicle, 50 μM PUGNAc or 50 μM OSMI-1. ChIP–sequencing tracks for SLC7A11 (**B**) and GPX4 (**C**) from HK-2 cells with different levels of O-GlcNAcylated BACH2. **D** The levels of SLC7A11 and GPX4 promoters binding to parental BACH2 were detected by ChIP–qPCR and normalized according to the result of IgG group ($n = 5$ group^{-1}); one-way ANOVA followed by Tukey's test. ChIP–qPCR results illustrating the interaction intensity of the parental BACH2 and T389A mutant on SLC7A11 (**E**) and GPX4 (**F**) promoters, after administration of vehicle, 50 μM PUGNAC or 50 μM OSMI-1 ($n = 5$ group^{-1}); one-way ANOVA followed by Tukey's test. Schematic representation of the binding sequences of BACH2 on SLC7A11 (**G**) and GPX4 (**H**) promoters. Luciferase reporter assays determining the binding specificities and transcriptional regulations of BACH2 on SLC7A11 (**I**) and GPX4 (**J**, $n = 5$ group^{-1}); one-way ANOVA followed by Tukey's test. Luciferase reporter results showing the effect of O-GlcNAcylation on BACH2-mediated transcriptional regulations on SLC7A11 (**K**) and GPX4 (**L**, $n = 5$ group^{-1}); one-way ANOVA followed by Tukey's test. ***$p < 0.001$, **$p < 0.01$, and *$p < 0.05$ represent significant differences between two groups; ns represents no significant difference.

GPX4 transcription resulting from BACH2 overexpression were both further intensified when the O-GlcNAc modification was facilitated by PUGNAc but dramatically weakened after administration of OSMI-1.

These findings have provided definitive evidence that O-GlcNAcylation further strengthens the repressive effect of BACH2 on SLC7A11 and GPX4 and thus promotes ferroptosis. Nevertheless, the detailed mechanisms by which BACH2 downregulates the transcriptional levels of SLC7A11 and GPX4 remain unclear. Therefore, we mapped genome-wide BACH2 binding sites by ChIP sequencing analysis. As shown in Fig. 6A, facilitating O-GlcNAcylation further increased the number of binding peaks on BACH2, which was partially reversed after OSMI-1 treatment. Importantly, we identified the binding locus of BACH2 in GPX4 (Fig. 6B) and SLC7A11 (Fig. 6C), and PUGNAc facilitated the binding activities on the locus. ChIP–qPCR assays further confirmed that BACH2 was bound to the "GGTGACTCAGTTCC" region on the GPX4 promoter and the "TCTCGACTCATTAC" region on the SLC7A11 promoter (Fig. 6D). Consistently, inducing BACH2 O-GlcNAcylation increased the intensity of interaction, but OSMI-1 had the opposite effect (Fig. 6E, F). To understand how BACH2 binding to the promoters of SLC7A11 and GPX4 governs their transcriptional activities, we performed a series of dual-luciferase reporter assays with reporters bearing GPX4 and SLC7A11 parental cDNA or a mutant at the BACH2-binding site (Fig. 6G, H). We found that supplementation with exogenous BACH2, to varying extents, decreased the transcriptional activities of parental SLC7A11 and GPX4 but not mutants (Fig. 6I, J). In addition, parental BACH2-mediated transcriptional repression of SLC7A11 and GPX4 was further aggravated by PUGNAc but sharply reversed after OSMI-1 treatment. Nevertheless, the regulatory effects of PUGNAc and OSMI-1 on the BACH2-T389A mutant were considerably weakened (Fig. 6K, L), indicating that O-GlcNAc modification at Thr389 of BACH2, a transcription repressor, facilitated the binding of BACH2 to the promoters of SLC7A11 and GPX4, thereby exacerbating their transcriptional suppression.

IRI-sEVs containing lncR-WAC-AS1 promote the nephritic and systemic propagation of the "wave of ferroptosis" during mouse kidney transplantation

Finally, we established mouse models of allograft kidney transplantation combined with various treatments with IRI-sEVs

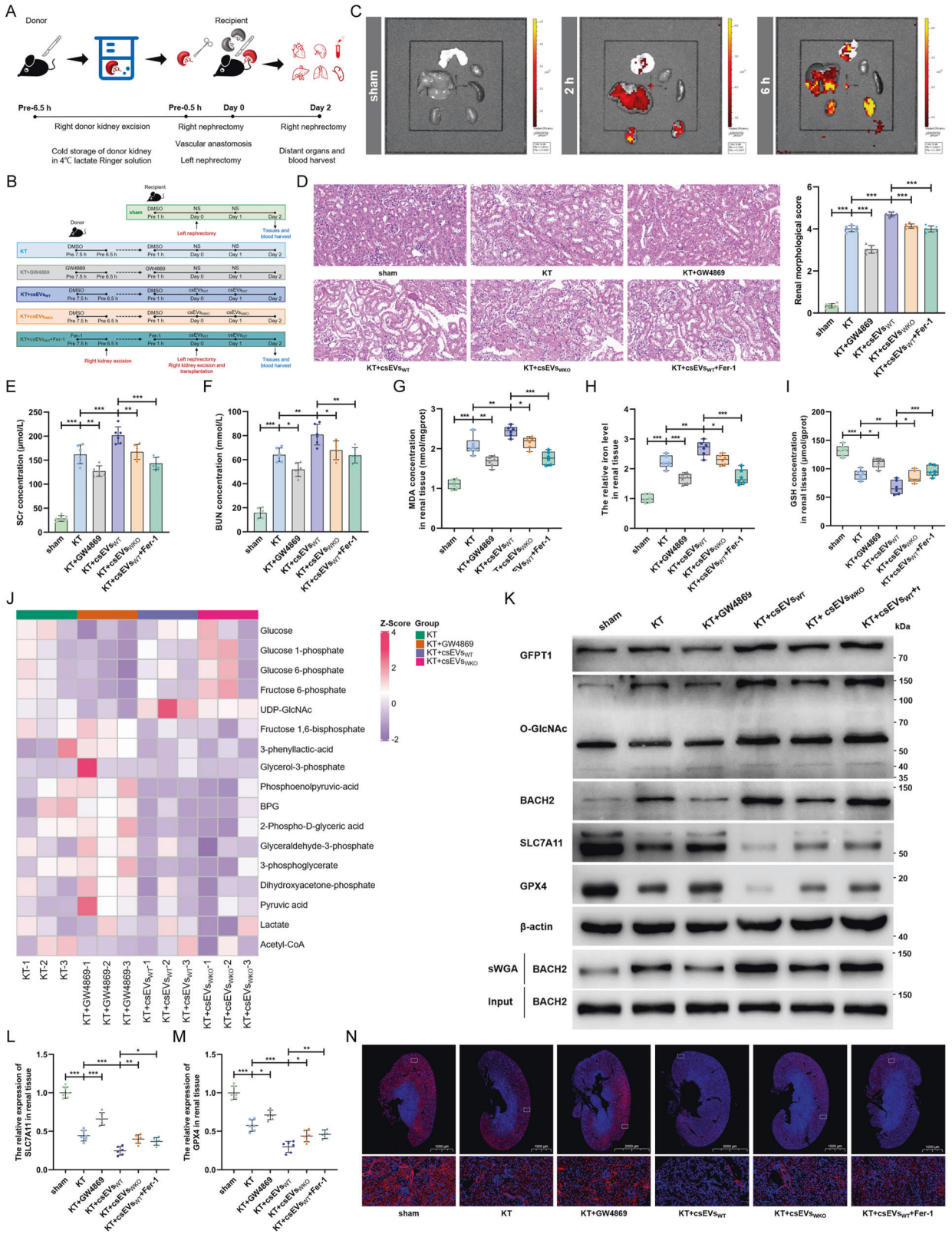

(csEVs$_{WT}$ and csEVs$_{WKO}$), GW4869 and ferrostatin-1 to further validate the findings in vivo (Fig. 7A, B). We first observed an increasing aggregation of exogenous PKH26-labeled IRI-sEVs in the kidney, liver and lung following tail intravenous injection, revealing the distribution tendency of sEVs among organs (Fig. 7C).

We subsequently detected the levels of lncRNA-WAC-AS1 in different organ-derived tsEVs (Supplementary File 1: Supplementary Fig. S11A–E) and ssEVs isolated from the circulatory system (Supplementary File 1: Fig. S11F–H) and found that renal IRI during transplantation not only increased the level of lncRNA-WAC-AS1 in

Fig. 7 IRI-sEVs containing lncR-WAC-AS1 facilitate ferroptosis propagation in graft during mouse allograft kidney transplantation. **A** Flowchart delineating the procedure of allograft kidney transplantation in WT C57BL/6 mouse. **B** Schematic representation of the experimental protocols in vivo. For inhibitor administration, donor mice received intraperitoneal injection of GW4869 (2.5 mg/kg), ferrostatin-1 (5 mg/kg) or DMSO 1 h before donor kidney excision, and recipient mice received the same administrations as paired donors 1 h before kidney transplantation. For csEV treatment, 100 μg of $csEVs_{WT}$, $csEVs_{WKO}$ or saline solution (NS) were injected by tail vein 0 h and 24 h after kidney transplantation ($n = 6$ group^{-1}). **C** The tracking of PKH26-labeled csEVs in different organs were imaged 2 h and 6 h after tail intravenous injection of 100 μg csEVs or NS by an IVIS Lumina imaging system. **D** HE staining (left) and renal pathological score (right) of renal tissue slice ($n = 6$ group^{-1}); scale bar: 20 μm; one-way ANOVA followed by Tukey's test. The SCr (**E**) and BUN (**F**) concentrations of mice after distinct treatments ($n = 6$ group^{-1}); one-way ANOVA followed by Tukey's test. MDA concentration (**G**), iron level (**H**) and GSH concentration (**I**) in graft renal tissues were normalized according to the level of sham ($n = 6$ group^{-1}); one-way ANOVA followed by Tukey's test. **J** LC-MS/MS metabolomics assays were performed to delineate the glucose-metabolite profiles of mouse graft kidneys in four groups ($n = 3$ group^{-1}). **K** The indicated proteins and O-GlcNAcylated levels in transplant kidneys were assessed by IB and sWGA pull-down assays. The translational levels of SLC7A11 (**L**) and GPX4 (**M**) in graft renal tissues ($n = 6$ group^{-1}); one-way ANOVA followed by Tukey's test. **N** IF assays detecting the expression level and region of SLC7A11 (red) in graft renal tissue slices; scale bar: 1000 μm and 2000 μm for the 1X and 20 μm for the 400X. ***$p < 0.001$, **$p < 0.01$, and *$p < 0.05$ represent significant differences between two groups.

renal-derived tsEVs but also induced elevations in tsEVs derived from the liver and lung and ssEVs but showed scarcely any effects on the myocardium and spleen. In addition, inhibition of endogenous EVs assembly and secretion by GW4869 considerably reduced lncRNA-WAC-AS1 in renal, lung and liver-derived tsEVs and ssEVs, while supplementation with exogenous IRI-sEVs derived from IRI WT-HK-2 cells ($csEVs_{WT}$) contributed to the dramatic elevations. These observations raised the possibility that IRI-sEVs, acting as active messengers, regulate renal IRI and even systemic injury by delivering lncRNA-WAC-AS1 in the kidney and circulation.

To test this possibility, we further detected that GW4869 sharply attenuated graft injury in morphology and function, as indicated by H&E staining (Fig. 7D) and the SCr and BUN concentrations (Fig. 7E, F). Reciprocally, $csEVs_{WT}$ further exacerbated graft injury after kidney transplantation, which was partially ameliorated after suppressing ferroptosis using ferrostatin-1. In addition, the decrease in lncRNA-WAC-AS1 in IRI-sEVs derived from IRI WKO cells ($csEVs_{WKO}$) weakened renal injury to some extent. Importantly, the regulatory effects of GW4869 and IRI-sEVs ($csEVs_{WT}$ and $csEVs_{WKO}$) on ferroptosis in renal tissues were broadly in line with the morphological and functional modulations (Fig. 7G–I). These findings suggest that endogenous and exogenous IRI-sEVs containing lncRNA-WAC-AS1 both prominently facilitate ferroptosis propagation in transplant kidneys and accordingly aggravate graft IRI.

To yield further mechanistic validation, we performed glucose metabolic profiling in graft kidneys, and the MS data showed that the UDP-GlcNAc content was downregulated when endogenous EVs were blocked by GW4869, whereas it was considerably elevated following supplementation with $csEVs_{WT}$ (Fig. 7J). The role of exogenous IRI-sEVs in inducing UDP-GlcNAc was notably blunted upon abrogation of lncRNA-WAC-AS1 in $csEVs_{WKO}$, suggesting that IRI-sEVs increase HBP fluxes and promote UDP-GlcNAc synthesis by delivering lncRNA-WAC-AS1. In addition, the expression of GFPT1 and O-GlcNAc and the level of O-GlcNAcylated BACH2 increased in parallel after the addition of $csEVs_{WT}$, accordingly contributing to BACH2 upregulation at the translational level (Fig. 7K and Supplementary File 2). In contrast, the results of IB (Fig. 7K and Supplementary File 2), qRT–PCR (Fig. 7L, M) and IF (Fig. 7N) assays showed that IRI-sEVs further suppressed the expression of SLC7A11 and GPX4 in renal tissues to promote ferroptosis. These in vivo results further corroborate the mechanism of IRI-sEV-induced the "wave of ferroptosis" propagation, by which lncRNA-WAC-AS1 enriched in IRI-sEVs facilitates HBP metabolic reprogramming and BACH2 O-GlcNAcylation in neighboring cell populations and thus strengthens BACH2-mediated suppression of SLC7A11 and GPX4.

We confirmed that renal IRI triggered the increased release of IRI-sEVs to the circulatory system and led to elevations in lncRNA-WAC-AS1 in distant organs (Supplementary File 1: Supplementary Fig. S11B, C). Therefore, we continued to explore whether IRI-sEVs fostered the "wave of ferroptosis" systemic propagation. Indeed, we found that renal IRI during transplantation inhibited the expression of SLC7A11 and GPX4 in the lung and thus promoted ferroptosis, which was diminished after impeding endogenous EV secretion but further exacerbated by supplementation with exogenous $csEVs_{WT}$ (Supplementary File 1: Supplementary Fig. S12A–E). Nevertheless, ferroptosis and the expression of SLC7A11 and GPX4 were hardly altered in other organs, including the liver (Supplementary File 1: Supplementary Fig. S12F–J), myocardium (Supplementary File 1: Supplementary Fig. S12K–O) and spleen (Supplementary File 1: Supplementary Fig. S12P–T). These findings imply that renal IRI-sEVs facilitate "wave of ferroptosis" propagation not only in the renal tissue microenvironment but also to distant lungs through the circulatory system.

DISCUSSION

The wide propagation of the "wave of ferroptosis" provokes extensive tubular necrosis, thus aggravating IR-induced renal injury and DGF during transplantation to a large extent [8, 43]. Nevertheless, the potential spread approaches and mechanisms underlying this phenomenon remain unclear. In this study, for the first time, we disclose the componential variation in usEVs derived from paired donors and recipients of kidney transplants and ascertain the central role of lncRNA-WAC-AS1 enriched in IRI-sEVs in facilitating the nephritic and systemic propagation of the "wave of ferroptosis". Mechanistically, we propose that lncRNA-WAC-AS1 promotes ferroptosis due to its metabolic regulation; that is, IRI-sEVs delivering lncRNA-WAC-AS1 foster HBP metabolic acceleration and BACH2 O-GlcNAcylation in neighboring and distant cell populations and thus potentiate the transcriptional suppression of SLC7A11 and GPX4 induced by BACH2, facilitating wide propagation of the "wave of ferroptosis" (Fig. 8).

Accumulating evidence demonstrates the predominance of ferroptosis in promoting tubular necrosis in the renal IRI process [44]. Of special importance, the wide propagation of ferroptosis, a pivotal feature distinguishing it from other forms of cell death, further provokes spatiotemporal patterns of cell death with an expanding scale and wave-like appearance and thereby exacerbates renal IRI [6, 8, 9, 45]. Emerging data have revealed that cells undergoing ferroptosis secrete a series of stimulating factors that act as signal propagators, inducing ferroptosis in neighboring cells in various ways. Nishizawa et al. revealed that the release of lipid peroxides and lipid hydroperoxyl radicals resulting from cell membrane rupture generated a lipid peroxidation gradient in the surrounding environment, thus causing ferroptotic signal propagation [43]. In addition, Michael Overholtzer et al. proposed a potential link between the "wave of ferroptosis" and ferroptotic cell swelling and rupture, and they demonstrated that the wave-like spread required the continuous stimulation of iron and lipid

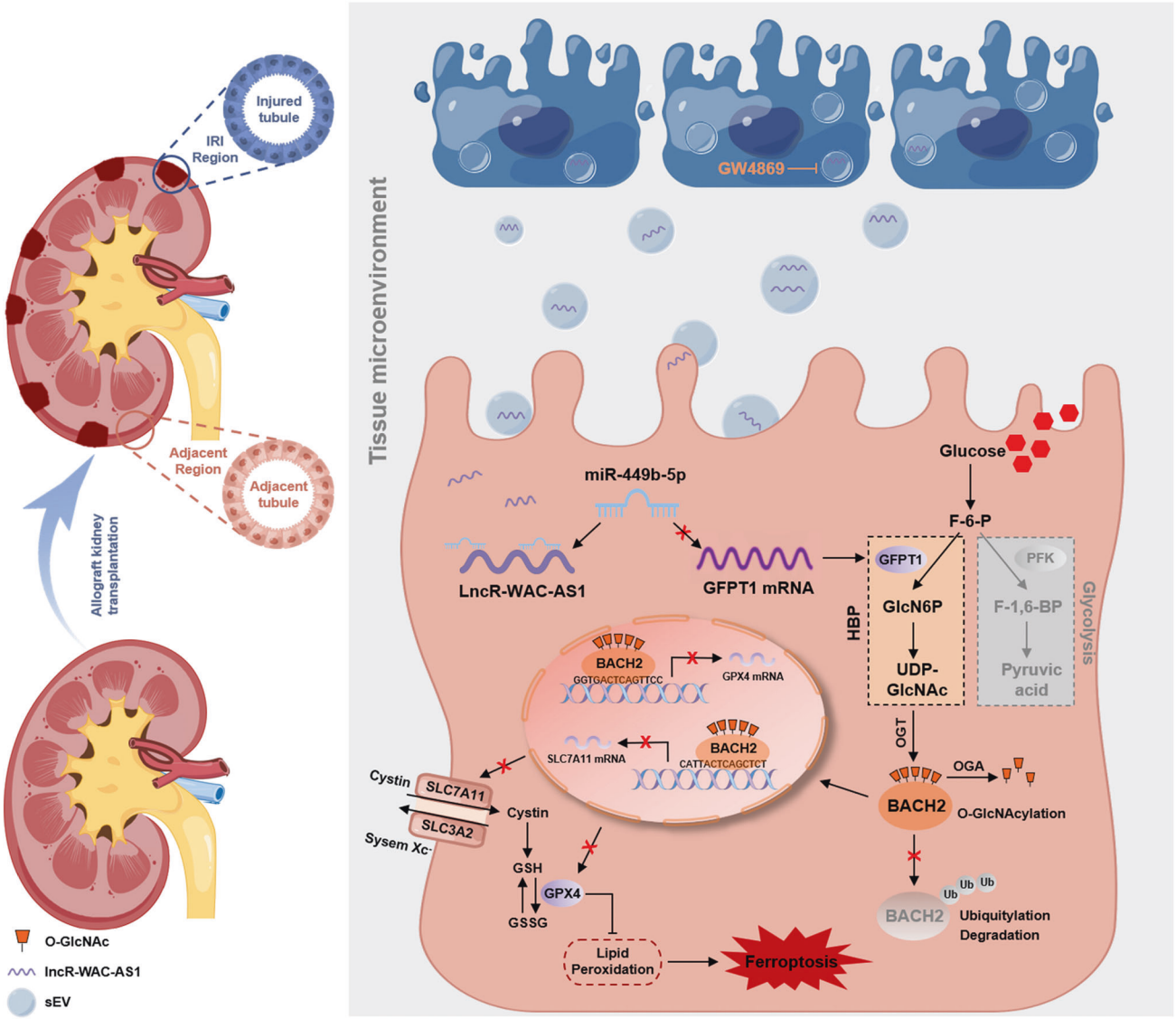

Fig. 8 Proposed model for how IRI-sEVs mediate the wide propagation of "wave of ferroptosis". LncRNA-WAC-AS1 enriched in IRI-sEVs facilitates HBP metabolic acceleration by upregulating GFPT1 and promotes BACH2 O-GlcNAcylation in neighboring and distant cell populations; this further enhances BACH2-mediated transcriptional suppression of SLC7A11 and GPX4, accordingly inducing ferroptosis spread.

peroxidation and involved upstream propagative signals of cell rupture, such as calcium flux [7, 11]. The in vivo data from Katikaneni also raised the possibility that ferroptotic cell-secreted arachidonic acid, a key driver of ferroptosis, can attract and directly affect redox signaling in leukocytes, thereby regulating inflammatory cues and a "wave of cell death" in intact zebrafish larvae [46]. Interestingly, a compelling series of studies recently indicated the pivotal role of ferroptotic cell-derived nanoparticles in ferroptosis development and propagation. For instance, the group of Michael Overholtzer found that high-dose particle delivery of poly(ethylene glycol)-coated silica nanoparticles (αMSH-PEG-C′dots) promoted intercellular ferroptosis propagation by delivering iron into neighboring cells and upregulating FTH1, which is responsible for binding cytosolic iron, thus inhibiting melanoma growth [47]. However, they felt that αMSH-PEG-C′dot-induced ferroptosis spread occurred regardless of GPX4 inhibition and bypassed the requirement for glutamine, which remains controversial. However, another study by Brown suggested that prominin 2 was upregulated to limit the intracellular accumulation of free iron under ferroptosis-inducing conditions, such as GPX4 inhibition and extracellular matrix detachment, by promoting the secretion of exosome trafficking of ferritin and iron [12]. Therefore, it remains unclear to what extent and how the nanoparticles secreted by cells undergoing ferroptosis induce the "wave of ferroptosis". In the present study, we first propose a novel mechanism by which IRI cell-secreted sEVs mediate intercellular ferroptosis propagation by delivering lncRNA-WAC-AS1 and inducing genetic and functional alterations in neighboring cells and distant lung cells. Interestingly, we observed a distribution tendency of IRI-sEVs mainly aggregating in the kidney, lung and liver, rather than the spleen and heart. It is probably because of the different tissue microenvironment which is important in yielding organ-specific distribution of EVs. For instance, the bone marrow, lung, brain, and liver parenchyma impose different selective pressures for EV populations, such as the distinct physiological barriers and haematogenous dynamics including circulation patterns and vascular wall accessibility [48, 49]. In addition, integrins, a large family of cell adhesion molecules, have been revealed to play a crucial role in dictating organ-specific targeting of EVs, accordingly determining organotropism to

specific organs [50]. Hoshino et al. demonstrated that sEV-derived integrin α6β4 and integrin α6β1 specify lung aggregation, while integrin αvβ5 directs sEVs to the liver and integrin β3 to the brain [51]. Therefore, the need for a further comprehensive analysis of IRI-sEV-induced ferroptosis propagation remains.

Mechanistically, mounting studies indicate that multiple cellular metabolic processes, including glucose, lipid, and amino acid metabolism, are tightly coupled with the cell's susceptibility to ferroptosis [52–54]. There has been particularly overwhelming interest in glucose metabolic reprogramming in the last few years due to its exceptional performance in antioxidant defense regulation. For example, decreasing the key metabolites and enzymes in the TCA cycle, including alpha-ketoglutarate, succinic acid and fumaric acid fumarate hydratase, has been demonstrated to suppress ferroptosis by reducing the generation of ROS in mitochondrial bioenergetic processes [22, 53]. In addition, metabolic rewiring from glycolysis to OXPHOS disrupted cellular iron homeostasis and facilitated lipid peroxidation by producing higher levels of ROS, which could be provisionally reversed by accelerating glycolytic flux [21]. Further evidence was elucidated in the study by Wang et al., in which the glycolytic rate was prominently slowed in cells treated with erastin or RSL3 (an inhibitor of GPX4), as determined by the reductions in key enzymes in the glycolysis pathway, such as hexokinase, phosphofructokinase and pyruvate kinase [55]. A recent study from Leu et al. also suggested that the glucose metabolic switch from glycolysis to PPP enhanced the NADPH/$NADP^+$ ratio by inhibiting the expression of activating transcription factor 4 to decrease cellular sensitivity toward ferroptosis under various stress conditions [23]. Based on summarized evidence, much less is known about the potential effect of HBP metabolism, another glucose-related pathway branching off from glycolysis, on ferroptosis regulation. Here, we present the first evidence that HBP metabolic acceleration considerably fosters ferroptosis by providing abundant UDP-GlcNAc for protein O-GlcNAc modification. The present study delineates a novel metabolic connection between glucose metabolic reprogramming and ferroptosis.

In parallel to the regulation of HBP metabolic flux, O-GlcNAcylation, acting as a nutrient sensor, is also highly sensitive to various stress stimuli, including IR. Recently, a growing body of studies has focused on the beneficial and detrimental effects of O-GlcNAcylation on diverse ischemic diseases, especially in patients with glucose metabolic disorders. Prakoso et al. found that excess glucose availability in hyperglycemia patients undergoing coronary artery bypass graft surgery boosted myocardial O-GlcNAcylation levels and thus reduced left ventricular ejection fraction [56]. Consistently, the increased UDP-GlcNAc and O-GlcNAcylation levels in hyperglycemic rats also provoked an evident impairment of cardiac contraction and relaxation [57]. Nevertheless, another study by Ou et al. revealed the cardioprotective effect of protein O-GlcNAc modification, that is, O-GlcNAcylation of glucose-6-phosphate dehydrogenase heightened hypoxic acclimation-induced antioxidative and cardioprotective effects and promoted redox homeostasis in IR myocardial cells [58]. Therefore, HBP metabolism-mediated O-GlcNAcylation has pleiotropic capacity in IRI regulation. In this study, we demonstrate, for the first time, that BACH2 O-GlcNAcylation at the Thr389 residue is dramatically elevated in IRI renal tissues through O-GlcNAcylation omics analysis and pinpointed that O-GlcNAc modification further potentiates BACH2-mediated transcriptional suppression of SLC7A11 and GPX4, accordingly fostering ferroptosis. This finding in the renal IRI process reveals a significant regulatory relationship between protein O-GlcNAcylation and ferroptosis propagation.

It has been well documented that BACH2 acts as an oxidative stress-responsive transcription repressor, induces oxidative stress-mediated apoptosis and modulates intracellular ROS production, which was determined by the increasing nuclear localization of BACH2 [59]. Multiple mechanisms were determined to affect the subcellular localization of BACH2, accordingly regulating the levels of intracellular ROS and apoptosis. In Ph-positive cells treated with imatinib, dephosphorylation of BACH2 promoted its nuclear translocation by attenuating a cytoplasmic localization signal regulated by Crm1/exportin1-dependent nuclear export and potentiated the transcriptional repression of heme oxygenase-1, inducing apoptosis in response to excessive cellular oxidation levels [60]. The small ubiquitin-like modifier-1 modification of BACH2 has also been demonstrated to increase the nuclear accumulation of BACH2 and participate in protein recruitment around the promyelocytic leukemia body, leading to an apoptotic response [41]. Although extensive studies have focused on the advantages of the BACH2 response to oxidative stress, less is known about its regulatory role in ferroptosis, which is also triggered under peroxidation conditions. Here, through ChIP-seq analysis and a series of validation experiments, we provide the first evidence that BACH2 prominently inhibits the transcriptional activities of SLC7A11 and GPX4, which are pivotal genes in the cyst(e)ine/GSH/GPX4 antioxidant system, and thus facilitates ferroptosis in the renal IRI process. In addition, we found that the O-GlcNAc modification of BACH2 fosters importin α5-mediated nuclear translocation depending on an NLS, which is indispensable for the transcriptional suppression of SLC7A11 and GPX4. However, other potential mechanisms underlying BACH2-induced ferroptosis and driving nuclear translocation remain to be elucidated.

In conclusion, we disclose a pivotal propagative approach of the "wave of ferroptosis" relying on IRI-sEVs in the renal IRI process and decipher a whole new metabolic mechanism underlying ferroptosis spread, that is, lncRNA-WAC-AS1 enriched in IRI-sEVs induces HBP metabolic reprogramming by upregulating GFPT1 and promotes BACH2 O-GlcNAcylation; this further potentiates the transcriptional suppression of SLC7A11 and GPX4 induced by BACH2, accordingly decreasing cellular anti-peroxidation capability and facilitating ferroptosis spread among normal renal tubular epithelial cells and even to distant lungs. These findings broaden our understanding of ferroptosis propagation in the renal IRI process and shed light on the potential of lncRNA-WAC-AS1 enriched in IRI-sEVs as a novel indicator and therapeutic target for IRI after kidney transplantation.

DATA AVAILABILITY

All data supporting the results reported here are available in the article and supplementary files or from the corresponding author upon reasonable request.

REFERENCES

1. Chen W, Wang L, Liang P, Mast J, Mathis C, Liu CY, et al. Reducing ischemic kidney injury through application of a synchronization modulation electric field to maintain Na(+)/K(+)-ATPase functions. Sci Transl Med. 2022;14:eabj4906.
2. Zhu J, Zhang G, Song Z, Xiang X, Shu S, Liu Z, et al. Protein kinase C-δ mediates kidney tubular injury in cold storage-associated kidney transplantation. J Am Soc Nephrol. 2020;31:1050–65.
3. Xu-Dubois YC, Ahmadpoor P, Brocheriou I, Louis K, Arzouk Snanoudj N, Rouvier P, et al. Microvasculature partial endothelial mesenchymal transition in early post-transplant biopsy with acute tubular necrosis identifies poor recovery renal allografts. Am J Transplant. 2020;20:2400–12.
4. Thompson ER, Bates L, Ibrahim IK, Sewpaul A, Stenberg B, McNeill A, et al. Novel delivery of cellular therapy to reduce ischemia reperfusion injury in kidney transplantation. Am J Transplant. 2021;21:1402–14.
5. Tonnus W, Meyer C, Steinebach C, Belavgeni A, von Mässenhausen A, Gonzalez NZ, et al. Dysfunction of the key ferroptosis-surveilling systems hypersensitizes mice to tubular necrosis during acute kidney injury. Nat Commun. 2021;12:4402.
6. Belavgeni A, Meyer C, Stumpf J, Hugo C, Linkermann A. Ferroptosis and necroptosis in the kidney. Cell Chem Biol. 2020;27:448–62.
7. Riegman M, Bradbury MS, Overholtzer M. Population dynamics in cell death: mechanisms of propagation. Trends Cancer. 2019;5:558–68.

8. Linkermann A, Skouta R, Himmerkus N, Mulay SR, Dewitz C, De Zen F, et al. Synchronized renal tubular cell death involves ferroptosis. Proc Natl Acad Sci USA. 2014;111:16836–41.
9. Martin-Sanchez D, Fontecha-Barriuso M, Carrasco S, Sanchez-Niño MD, Mässenhausen AV, Linkermann A, et al. TWEAK and RIPK1 mediate a second wave of cell death during AKI. Proc Natl Acad Sci USA. 2018;115:4182–7.
10. Vanden Berghe T, Linkermann A, Jouan-Lanhouet S, Walczak H, Vandenabeele P. Regulated necrosis: the expanding network of non-apoptotic cell death pathways. Nat Rev Mol Cell Biol. 2014;15:135–47.
11. Riegman M, Sagie L, Galed C, Levin T, Steinberg N, Dixon SJ, et al. Ferroptosis occurs through an osmotic mechanism and propagates independently of cell rupture. Nat Cell Biol. 2020;22:1042–8.
12. Brown CW, Amante JJ, Chhoy P, Elaimy AL, Liu H, Zhu LJ, et al. Prominin2 drives ferroptosis resistance by stimulating iron export. Dev Cell. 2019;51:575–86.e574.
13. van Niel G, Carter DRF, Clayton A, Lambert DW, Raposo G, Vader P. Challenges and directions in studying cell-cell communication by extracellular vesicles. Nat Rev Mol cell Biol. 2022;23:369–82.
14. van der Pol E, Böing AN, Harrison P, Sturk A, Nieuwland R. Classification, functions, and clinical relevance of extracellular vesicles. Pharmacol Rev. 2012;64:676–705.
15. Huang D, Sun G, Hao X, He X, Zheng Z, Chen C et al. ANGPTL2-containing small extracellular vesicles from vascular endothelial cells accelerate leukemia progression. J Clin Invest. 2021;131:e138986.
16. Liu W, Tang P, Wang J, Ye W, Ge X, Rong Y, et al. Extracellular vesicles derived from melatonin-preconditioned mesenchymal stem cells containing USP29 repair traumatic spinal cord injury by stabilizing NRF2. J Pineal Res. 2021;71:e12769.
17. Zhao H, Chen X, Hu G, Li C, Guo L, Zhang L, et al. Small extracellular vesicles from brown adipose tissue mediate exercise cardioprotection. Circulation Res. 2022;130:1490–506.
18. Gan L, Xie D, Liu J, Bond Lau W, Christopher TA, Lopez B, et al. Small extracellular microvesicles mediated pathological communications between dysfunctional adipocytes and cardiomyocytes as a novel mechanism exacerbating ischemia/reperfusion injury in diabetic mice. Circulation. 2020;141:968–83.
19. Ge X, Meng Q, Wei L, Liu J, Li M, Liang X, et al. Myocardial ischemia-reperfusion induced cardiac extracellular vesicles harbour proinflammatory features and aggravate heart injury. J Extracell Vesicles. 2021;10:e12072.
20. Liu J, Peng Y, Shi L, Wan L, Inuzuka H, Long J, et al. Skp2 dictates cell cycle-dependent metabolic oscillation between glycolysis and TCA cycle. Cell Res. 2021;31:80–93.
21. Marchiq I, Le Floch R, Roux D, Simon MP, Pouyssegur J. Genetic disruption of lactate/H+ symporters (MCTs) and their subunit CD147/BASIGIN sensitizes glycolytic tumor cells to phenformin. Cancer Res. 2015;75:171–80.
22. Gao M, Yi J, Zhu J, Minikes AM, Monian P, Thompson CB, et al. Role of mitochondria in ferroptosis. Mol Cell. 2019;73:354–63.e353.
23. Leu JI, Murphy ME, George DL. Functional interplay among thiol-based redox signaling, metabolism, and ferroptosis unveiled by a genetic variant of TP53. Proc Natl Acad Sci USA. 2020;117:26804–11.
24. Stincone A, Prigione A, Cramer T, Wamelink MM, Campbell K, Cheung E, et al. The return of metabolism: biochemistry and physiology of the pentose phosphate pathway. Biol Rev Camb Philos Soc. 2015;90:927–63.
25. Gao M, Monian P, Quadri N, Ramasamy R, Jiang X. Glutaminolysis and transferrin regulate ferroptosis. Mol Cell. 2015;59:298–308.
26. Yan B, Ai Y, Sun Q, Ma Y, Cao Y, Wang J, et al. Membrane damage during ferroptosis is caused by oxidation of phospholipids catalyzed by the oxidoreductases POR and CYB5R1. Mol cell. 2021;81:355–69.e310.
27. Lam C, Low JY, Tran PT, Wang H. The hexosamine biosynthetic pathway and cancer: current knowledge and future therapeutic strategies. Cancer Lett. 2021;503:11–18.
28. Gélinas R, Mailleux F, Dontaine J, Bultot L, Demeulder B, Ginion A, et al. AMPK activation counteracts cardiac hypertrophy by reducing O-GlcNAcylation. Nat Commun. 2018;9:374.
29. Mapanga RF, Joseph D, Symington B, Garson KL, Kimar C, Kelly-Laubscher R, et al. Detrimental effects of acute hyperglycaemia on the rat heart. Acta Physiologica. 2014;210:546–64.
30. Mapanga RF, Essop MF. Damaging effects of hyperglycemia on cardiovascular function: spotlight on glucose metabolic pathways. Am J Physiol Heart Circulatory Physiol. 2016;310:H153–173.
31. Cong R, Sun L, Yang J, Cui H, Ji X, Zhu J, et al. Protein O-GlcNAcylation alleviates small intestinal injury induced by ischemia-reperfusion and oxygen-glucose deprivation. Biomed Pharmacother. 2021;138:111477.
32. Li X, Peng X, Zhang C, Bai X, Li Y, Chen G, et al. Bladder cancer-derived small extracellular vesicles promote tumor angiogenesis by inducing HBP-related metabolic reprogramming and SerRS O-GlcNAcylation in endothelial cells. Adv Sci. 2022;9:e2202993.
33. Théry C, Witwer KW, Aikawa E, Alcaraz MJ, Anderson JD, Andriantsitohaina R, et al. Minimal information for studies of extracellular vesicles 2018 (MISEV2018): a position statement of the International Society for Extracellular Vesicles and update of the MISEV2014 guidelines. J Extracell Vesicles. 2018;7:1535750.
34. Dhondt B, Geeurickx E, Tulkens J, Van Deun J, Vergauwen G, Lippens L, et al. Unravelling the proteomic landscape of extracellular vesicles in prostate cancer by density-based fractionation of urine. J Extracell Vesicles. 2020;9:1736935.
35. Jingushi K, Uemura M, Ohnishi N, Nakata W, Fujita K, Naito T, et al. Extracellular vesicles isolated from human renal cell carcinoma tissues disrupt vascular endothelial cell morphology via azurocidin. Int J cancer. 2018;142:607–17.
36. Guo J, Wu C, Lin X, Zhou J, Zhang J, Zheng W, et al. Establishment of a simplified dichotomic size-exclusion chromatography for isolating extracellular vesicles toward clinical applications. J Extracell Vesicles. 2021;10:e12145.
37. Li X, Wei Z, Yu H, Xu Y, He W, Zhou X, et al. Secretory autophagy-induced bladder tumour-derived extracellular vesicle secretion promotes angiogenesis by activating the TPX2-mediated phosphorylation of the AURKA-PI3K-AKT axis. Cancer Lett. 2021;523:10–28.
38. Minami K, Bae S, Uehara H, Zhao C, Lee D, Iske J, et al. Targeting of intragraft reactive oxygen species by APP-103, a novel polymer product, mitigates ischemia/reperfusion injury and promotes the survival of renal transplants. Am J Transplant. 2020;20:1527–37.
39. Yoshida C, Yoshida F, Sears DE, Hart SM, Ikebe D, Muto A, et al. Bcr-Abl signaling through the PI-3/S6 kinase pathway inhibits nuclear translocation of the transcription factor Bach2, which represses the antiapoptotic factor heme oxygenase-1. Blood. 2007;109:1211–9.
40. Zhou Y, Wu H, Zhao M, Chang C, Lu Q. The Bach family of transcription factors: a comprehensive review. Clin Rev allergy Immunol. 2016;50:345–56.
41. Kono K, Harano Y, Hoshino H, Kobayashi M, Bazett-Jones DP, Muto A, et al. The mobility of Bach2 nuclear foci is regulated by SUMO-1 modification. Exp Cell Res. 2008;314:903–13.
42. Hoshino H, Kobayashi A, Yoshida M, Kudo N, Oyake T, Motohashi H, et al. Oxidative stress abolishes leptomycin B-sensitive nuclear export of transcription repressor Bach2 that counteracts activation of Maf recognition element. J Biol Chem. 2000;275:15370–6.
43. Nishizawa H, Matsumoto M, Chen G, Ishii Y, Tada K, Onodera M, et al. Lipid peroxidation and the subsequent cell death transmitting from ferroptotic cells to neighboring cells. Cell Death Dis. 2021;12:332.
44. Wang J, Liu Y, Wang Y, Sun L. The cross-link between ferroptosis and kidney diseases. Oxid Med Cell Longev. 2021;2021:6654887.
45. Linkermann A, Hackl MJ, Kunzendorf U, Walczak H, Krautwald S, Jevnikar AM. Necroptosis in immunity and ischemia-reperfusion injury. Am J Transplant. 2013;13:2797–804.
46. Katikaneni A, Jelcic M, Gerlach GF, Ma Y, Overholtzer M, Niethammer P. Lipid peroxidation regulates long-range wound detection through 5-lipoxygenase in zebrafish. Nat Cell Biol. 2020;22:1049–55.
47. Kim SE, Zhang L, Ma K, Riegman M, Chen F, Ingold I, et al. Ultrasmall nanoparticles induce ferroptosis in nutrient-deprived cancer cells and suppress tumour growth. Nat Nanotechnol. 2016;11:977–85.
48. Urabe F, Patil K, Ramm GA, Ochiya T, Soekmadji C. Extracellular vesicles in the development of organ-specific metastasis. J Extracell Vesicles. 2021;10:e12125.
49. Nguyen DX, Bos PD, Massagué J. Metastasis: from dissemination to organ-specific colonization. Nat Rev Cancer. 2009;9:274–84.
50. Park EJ, Shimaoka M. Integrin-mediated exosomal homing to organs. Methods Mol Biol. 2023;2668:145–58.
51. Hoshino A, Costa-Silva B, Shen TL, Rodrigues G, Hashimoto A, Tesic Mark M, et al. Tumour exosome integrins determine organotropic metastasis. Nature. 2015;527:329–35.
52. Liang D, Minikes AM, Jiang X. Ferroptosis at the intersection of lipid metabolism and cellular signaling. Mol Cell. 2022;82:2215–27.
53. Yao X, Li W, Fang D, Xiao C, Wu X, Li M, et al. Emerging roles of energy metabolism in ferroptosis regulation of tumor cells. Adv Sci. 2021;8:e2100997.
54. Zheng J, Conrad M. The metabolic underpinnings of ferroptosis. Cell Metab. 2020;32:920–37.
55. Wang X, Lu S, He C, Wang C, Wang L, Piao M, et al. RSL3 induced autophagic death in glioma cells via causing glycolysis dysfunction. Biochem Biophys Res Commun. 2019;518:590–7.
56. Prakoso D, Lim SY, Erickson JR, Wallace RS, Lees JG, Tate M, et al. Fine-tuning the cardiac O-GlcNAcylation regulatory enzymes governs the functional and structural phenotype of the diabetic heart. Cardiovasc Res. 2022;118:212–25.
57. Fülöp N, Mason MM, Dutta K, Wang P, Davidoff AJ, Marchase RB, et al. Impact of Type 2 diabetes and aging on cardiomyocyte function and O-linked N-acetylglucosamine levels in the heart. Am J Physiol Cell Physiol. 2007;292:C1370–8.
58. Ou W, Liang Y, Qin Y, Wu W, Xie M, Zhang Y, et al. Hypoxic acclimation improves cardiac redox homeostasis and protects heart against ischemia-reperfusion injury through upregulation of O-GlcNAcylation. Redox Biol. 2021;43:101994.

59. Hoshino H, Igarashi K. Expression of the oxidative stress-regulated transcription factor bach2 in differentiating neuronal cells. J Biochem. 2002;132:427–31.
60. Suzuki H, Tashiro S, Sun J, Doi H, Satomi S, Igarashi K. Cadmium induces nuclear export of Bach1, a transcriptional repressor of heme oxygenase-1 gene. J Biol Chem. 2003;278:49246–53.

ACKNOWLEDGEMENTS

We appreciate Researcher Xin Liu at the CAS Centre for Excellence in Molecular Cell Science for the technical assistance. We also thank the New Talent Program initiated by Chongqing Medical University. This work was supported by the National Natural Science Foundation of China under Grant (number: 81874092) and Chongqing Science and Technology Bureau under Grant (number: cstc2019jscx-dxwtBX0018).

AUTHOR CONTRIBUTIONS

Conceptualization: XL; Methodology: XL, XP and XZ; Investigation: XL, XP, ML, GC, WS, HY, CZ, YL and ZF; Writing-Original Draft: XL; Funding Acquisition: WH and XG; Resources: SL, WH and XG; Supervision: WH and XG; Revision: XL, XZ and JL.

COMPETING INTERESTS

The authors declare no competing interests.

ETHICS

The study was approved by the Medical Ethics Committee of the First Affiliated Hospital of Chongqing Medical University (181). The clinical and research activities being reported are consistent with the Principles of the Declaration of Istanbul as outlined in the "Declaration of Istanbul on Organ Trafficking and Transplant Tourism". All animal experimental protocols and care procedures conformed to the Chongqing Medical University of Medicine Policy on the Care and Use of Laboratory Animals (k276).

ADDITIONAL INFORMATION

Supplementary information The online version contains supplementary material available at https://doi.org/10.1038/s41418-023-01198-x.

Correspondence and requests for materials should be addressed to Weiyang He or Xin Gou.

Reprints and permission information is available at http://www.nature.com/reprints

Publisher's note Springer Nature remains neutral with regard to jurisdictional claims in published maps and institutional affiliations.